INSTITUT DE FRANCE
Académie des sciences

Comptes Rendus

Physique

V. Romero-García, N. Jiménez, G. Theocharis, V. Achilleos, A. Merkel, O. Richoux, V. Tournat, J.-P. Groby and V. Pagneux

Design of acoustic metamaterials made of Helmholtz resonators for perfect absorption by using the complex frequency plane

Volume 21, issue 7-8 (2020), p. 713-749.

<https://doi.org/10.5802/crphys.32>

Part of the Thematic Issue: Metamaterials 2

Guest editors: Boris Gralak (CNRS, Institut Fresnel, Marseille, France) and Sébastien Guenneau (UMI2004 Abraham de Moivre, CNRS-Imperial College, London, UK)

Les Comptes Rendus. Physique *sont membres du Centre Mersenne pour l'édition scientifique ouverte*
www.centre-mersenne.org

Comptes Rendus
Physique
2020, 21, nº 7-8, p. 713-749
https://doi.org/10.5802/crphys.32

Metamaterials 2 / *Métamatériaux 2*

Design of acoustic metamaterials made of Helmholtz resonators for perfect absorption by using the complex frequency plane

Conception de métamatériaux acoustiques constitués de résonateurs de Helmholtz pour l'absorption parfaite dans le plan des fréquences complexes

V. Romero-García*, [a], N. Jiménez [a], G. Theocharis [a], V. Achilleos [a], A. Merkel [a], O. Richoux [a], V. Tournat [a], J.-P. Groby [a] and V. Pagneux [a]

[a] Laboratoire d'Acoustique de l'Université du Mans (LAUM), UMR 6613, Institut d'Acoustique - Graduate School (IA-GS), CNRS, Le Mans Université, France

Current addresses: I3M, Instituto de Instrumetación para Imagen Molecular, CSIC - Universitat Politècnica de València, València, Spain (N. Jiménez), Université de Lorraine, CNRS, Institut Jean Lamour, F-54000 Nancy, France (A. Merkel)

E-mails: vicente.romero@univ-lemans.fr (V. Romero-García), nojigon@upv.es (N. Jiménez), Georgios.Theocharis@univ-lemans.fr (G. Theocharis), Achilleos.Vassos@univ-lemans.fr (V. Achilleos), aurelien.merkel@univ-lemans.fr (A. Merkel), olivier.richoux@univ-lemans.fr (O. Richoux), vincent.tournat@univ-lemans.fr (V. Tournat), Jean-Philippe.Groby@univ-lemans.fr (J.-P. Groby), Vincent.Pagneux@univ-lemans.fr (V. Pagneux)

Abstract. In this review, we present the results on sub-wavelength perfect acoustic absorption using acoustic metamaterials made of Helmholtz resonators with different setups. Low frequency perfect absorption requires to increase the number of states at low frequencies and finding the good conditions for impedance matching with the background medium. If, in addition, one wishes to reduce the geometric dimensions of the proposed structures for practical issues, one can use properly designed local resonators and achieve sub-wavelength perfect absorption. Helmholtz resonators have been shown good candidates due to their easy tunability of the geometry, so of the resonance frequency, the energy leakage and the intrinsic losses. When plugged to a waveguide or a surrounding medium they behave as open, lossy and resonant systems characterized by their energy leakage and intrinsic losses. The balance between these two represents the critical coupling condition and gives rise to maximum energy absorption. The critical coupling mechanism is represented here in the complex frequency plane in order to interpret the impedance matching condition. In this

* Corresponding author.

review we discuss in detail the possibility to obtain perfect absorption by these critical coupling conditions in different systems such as reflection (one-port), transmission (two-ports) or three-ports systems.

Résumé. Dans cette revue, nous présentons des résultats sur l'absorption acoustique parfaite sub-longueur d'onde faisant appel à des métamatériaux acoustiques avec des résonateurs Helmholtz pour différentes configurations. L'absorption parfaite à basse fréquence nécessite une augmentation du nombre d'états aux basses fréquences ainsi que de trouver les bonnes conditions pour une adaptation d'impédance avec le milieu environnant. Si en outre, on souhaite réduire les dimensions géométriques des structures proposées pour des questions pratiques, on peut utiliser des résonateurs locaux judicieusement conçus afin d'attendre une absorption parfaite sub-longueur d'onde. Les résonateurs de Helmholtz se sont révélés de bons candidats en raison de leur accordabilité aisée de la géométrie, donc de la fréquence de résonance, de la fuite d'énergie et des pertes intrinsèques. Lorsqu'ils sont branchés à un guide d'ondes ou à un milieu environnant, ils se comportent comme des systèmes ouverts, avec pertes et résonances caractérisés par leur fuite d'énergie et leurs pertes intrinsèques. L'équilibre entre ces deux aspects représente la condition de couplage critique et donne lieu à un maximum d'absorption d'énergie. Le mécanisme de couplage critique est ici représenté dans le plan de fréquence complexe afin d'interpréter la condition d'adaptation d'impédance. Dans cette revue, nous discutons en détail la possibilité d'obtenir une absorption parfaite par ces conditions de couplage critiques dans différents systèmes tels que la réflexion (à un port), la transmission (à deux ports) ou les systèmes à trois ports.

Keywords. Acoustic metamaterials, Perfect absorption, Helmholtz resonators, Locally resonant materials, Critical coupling, Complex frequency plane.

Mots-clés. Métamatériaux acoustiques, Absorption parfaite, Résonateurs de Helmholtz, Résonateurs locaux, Couplage critique, Plan des fréquences complexes.

1. Introduction

The ability to perfectly absorb an incoming wave field in a sub-wavelength material is advantageous for several applications in wave physics as energy conversion [1], time reversal technology [2], coherent perfect absorbers [3] or soundproofing [4] among others. The solution of this challenge requires to solve a complex problem: reducing the geometric dimensions of the structure while increasing the number of states at low frequencies and finding the good conditions to match the impedance to the background medium.

A successful approach for increasing the number states at low frequencies with reduced dimensions is the use of metamaterials. Although the definition of metamaterial is still a source of discussion within the community, in this article, we will name metamaterial a structured system made of resonant elements with physical properties not usually encountered for wavelengths much larger than its dimensions. Exponentially increasing attention has been paid to these systems in all the fields of wave physics as electromagnetics [5], acoustics [6], elastodynamics [7, 8] and seismology [9], among others. In acoustics, the concept of metamaterial was introduced in the 2000s by Liu *et al.* [10] and Fang *et al.* [11]. Applications cover all frequency ranges from low-frequency vibrations to radio frequencies [6, 12]. Several possibilities based on these locally resonant systems have been recently proposed to design sound absorbing structures with simultaneous sub-wavelength dimensions and strong acoustic absorption [13–18]. Some strategies to design these sub-wavelength systems consist of using space-coiling structures [19–22], membranes [23], reconfigurable structures [24, 25] or Helmholtz resonators (HRs) [11, 26, 27]. However, all of these structures face the challenge of impedance mismatch to the background medium while they bring potentially solutions to reduce the geometric dimensions. Recently, several possibilities based on these systems made of open lossy resonant building blocks have been proposed to design sound absorbing structures with impedance match conditions, presenting simultaneously sub-wavelength dimensions and perfect acoustic absorption. Examples

are acoustic metamaterials made of membranes [13, 28–31], quater wavelength resonators [32], bubbles in water [33], aerogel plates [34], split ring resonators [35] or HRs [20, 28, 36–51]. Among them, HRs have been shown as potential candidates to solve the problem due to the tunable possibilities they offer just by optimizing their geometry. In this work, the resonance frequency, the energy leakage and the intrinsic losses can be passively tuned by the geometry of the resonator. In fact, the energy leakage of the HRs can be controlled by the aperture of the neck and the inherent viscothermal losses in the neck and in the cavity. We also show an example of nonlinear absorption in which the losses are driven dynamically with the amplitude of the incident wave.

The interaction of an incoming wave with an open, lossy and resonant structure, in particular the impedance matching with the background field, is one of the most studied process in the field of wave physics [1–3]. These open systems, at the resonant frequency, are characterized by both the leakage rate of energy (i.e., the coupling of the resonant elements with the propagating medium), and the intrinsic losses of the resonator. The balance between the leakage and the losses activates the condition of critical coupling, trapping the energy around the resonant elements and generating a maximum of energy absorption [36, 52]. In the case of a reflecting system (one port systems), either symmetric or antisymmetric resonances that are critically coupled can be used to obtain perfect absorption (PA) of energy [28, 29, 33, 37]. In the case of transmission systems with N-ports [53], the problems becomes more difficult. In particular for the two port case, degenerate critically coupled resonators with symmetric and antisymmetric resonances [30, 51, 54] or systems with broken symmetry [39, 42] can be used to perfectly absorb the incoming energy. At this stage it is worth noting what we consider as symmetry. If either the geometry of the resonator or the profile of the wave field are mirror symmetric (antisymmetric) with respect to the middle plane of the resonator, then the system will be considered as symmetric (antisymmetric).

In this review we discuss the technique based on the analysis of the zeros and poles of the eigenvalues of the scattering matrix. In general these zeros and poles correspond to complex frequencies, then we introduce a representation in the complex frequency plane, i.e., real versus imaginary part of the complex frequency, applied to the case of acoustic metamaterials made of HRs for deep sub-wavelength PA. This methodology has been shown as an efficient tool to design broadband acoustic absorbers in the low frequency range. In our case, fine tuning of both the losses and of the geometric characteristics of the sub-wavelength resonators lead to the crossing of the complex zeros of the eigenvalues of the scattering matrix with the real frequency axis, i.e., they appear at purely real frequencies, which signifies the PA condition. This methodology has been also used to design efficient broadband absorbers in the low frequency regime. Different systems corresponding to different configurations are studied in this work: single port configuration in which corresponds to the pure reflection problem; two port systems in which the transmission problem with single side excitation can be analyzed; and multiport systems, in particular a 3-port system. Several examples of perfect and broadband absorption in all of these configurations are reviewed in detail in this work.

2. Scattering problem in 1D systems

2.1. *General problem*

Let us consider a two-port, one-dimensional and reciprocal scattering process. The relation between the amplitudes of the incoming (a, d), and outcoming (b, c) waves, on both sides of

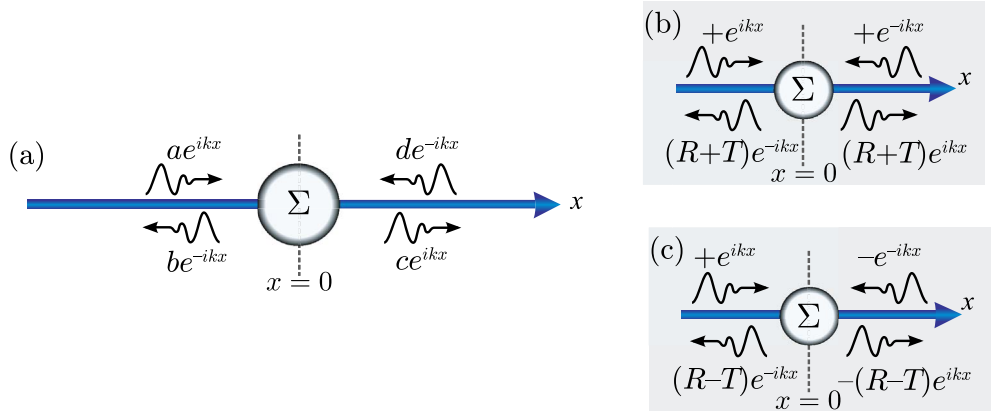

Figure 1. (a) Schematic of the two-port scattering process. (b) Symmetric and (c) antisymmetric uncoupled sub-problems for the case of a mirror-symmetric scatterer Σ. The time convention is $e^{-i\omega t}$. The weve number is $k = \omega/c$ with c the acoustic wave speed.

the scatterer Σ, as shown in Figure 1(a), is given by

$$\begin{pmatrix} c \\ b \end{pmatrix} = \mathbf{S}(f) \begin{pmatrix} a \\ d \end{pmatrix} = \begin{pmatrix} T & R^+ \\ R^- & T \end{pmatrix} \begin{pmatrix} a \\ d \end{pmatrix}, \tag{1}$$

where $\mathbf{S}(f)$ is the scattering matrix (S-matrix), f is the incident wave frequency, T is the complex amplitude transmission coefficient, R^- and R^+ are the complex amplitude reflection coefficients for left (−) and right (+) incidence, respectively. Note that the power scattering coefficients are, $|R^+|^2$, $|R^-|^2$ and $|T|^2$. In this work, the time dependence convention of the harmonic regime is $e^{-i\omega t}$, and it will be omitted in the following. The eigenvalues of the S-matrix are expressed as

$$\lambda_{1,2} = T \pm [R^- R^+]^{1/2} \tag{2}$$

and the eigenvectors of the system are

$$\begin{aligned} \mathbf{v_1} &= (v_{11}, v_{12}) = \left(R^+, -\sqrt{R^+R^-}\right) \\ \mathbf{v_2} &= (v_{21}, v_{22}) = \left(\sqrt{R^+R^-}, R^+\right). \end{aligned} \tag{3}$$

Therefore, the ratio of the eigenvector components v_{1i} and v_{2i} is $v_{2i}/v_{1i} = (-1)^i (R^-/R^+)^{1/2}$. A zero eigenvalue of the S-matrix corresponds to the case in which the incident waves corresponding to the eigenvectors of the S-matrix can be completely absorbed ($b = c = 0$). This, called coherent perfect absorption (CPA) [55], happens when $T = \pm[R^- R^+]^{1/2}$ and the incident waves a, d correspond to the relevant eigenvector.

Mirror symmetric scatterer

If the scatterer Σ is mirror symmetric with respect to the $x = 0$ plane, $R^+ = R^- \equiv R$ and the problem can be reduced to two uncoupled sub-problems by choosing incident waves that are symmetric (see Figure 1(b)) or antisymmetric (see Figure 1(c)) with the reflection coefficients $R_s = R + T$ and $R_a = R - T$. In particular, the reflection and transmission coefficients of the initial problem in Figure 1(a) can be expressed as $R = (R_s + R_a)/2$, and $T = (R_s - R_a)/2$ while the eigenvalues of the S-matrix can be written as $\lambda_1 = R_s$ and $\lambda_2 = -R_a$. For a one-sided incident wave, the absorption coefficient defined as $\alpha = 1 - |R|^2 - |T|^2$ becomes $\alpha = (\alpha_s + \alpha_a)/2$, where

$\alpha_s \equiv 1-|R_s|^2$ and $\alpha_a \equiv 1-|R_a|^2$. Achieving $\alpha(f_{\max})=1$ at a frequency $f_{\max}$, is equivalent to getting simultaneously the minima of the reflection coefficients of the two sub-problems, i.e., $R_a(f_{\max}) = R_s(f_{\max}) = 0$ [$\alpha_s(f_{\max}) = \alpha_a(f_{\max}) = 1$]. This has been achieved in Ref. [54] for a mirror symmetric slab made of graphene and a photonic crystal through intensive numerical calculations. In acoustics, these degenerate resonators have been analyzed and realized in Refs. [30, 51, 54].

Point symmetric scatterer

We now further consider that Σ is a point scatterer, i.e., its length is reduced to $x = 0$. In other words, the wavelength corresponding to the working frequency is much larger than the characteristic dimension of the resonator, which is the radius of the neck of a HR. This case is also relevant to the study of absorption by deep sub-wavelength scatterers. Imposing the continuity of the wave-field at this point [42] yields $1 + R = T$. This corresponds to $R_a = -1$, i.e., the scatterer Σ is transparent to antisymmetric incident waves, $\alpha_a = 0$, and thus $\alpha = \alpha_s/2 \leq 1/2$. The maximum value of one-sided absorption, appears at $f_{\max}$, is $\alpha(f_{\max}) = 1/2$. It corresponds to $\alpha_s(f_{\max}) = 1$ which gives $R_s(f_{\max}) = \lambda_1(f_{\max}) = 0$, and $R(f_{\max}) = -T(f_{\max}) = 1/2$. Thus, $\alpha(f_{\max}) = 1/2$ corresponds to CPA to the two-incident waves problem for symmetric and in phase incoming waves at $f_{\max}$, i.e., $v_2(f_{\max})/v_1(f_{\max}) = 1$ [56].

Mirror asymmetric scatterer

In the most general case Σ could be asymmetric, such that $R^+ \neq R^-$. In this case two absorption coefficients can be defined, $\alpha^+ = 1-|T|^2-|R^+|^2$ and $\alpha^- = 1-|T|^2-|R^-|^2$. When the eigenvalues of the scattering matrix are zero, $T = \pm\sqrt{R^+R^-}$. Therefore as soon as one of the reflection coefficients reaches zero, $T = 0$ and the system can present unidirectional perfect one-side absorption (UNPOA). The eigenvectors of the system will be represented by $\mathbf{v_1} = (R^+, -\sqrt{R^+R^-})$ and $\mathbf{v_2} = (\sqrt{R^+R^-}, R^+)$. From the analysis of the eigenvectors, the direction from which PA is obtained corresponds to an eigenvector equal to $(0,0)$. This situation has been exploited in acoustics to design UNPOA units [42, 45] and UNPOA panels [39].

2.2. *Complex frequency plane*

In the previous section we have highlighted the relevance of the eigenvalues and eigenvectors of the scattering matrix to identify the situations of PA in the system. A graphical procedure with rich information consists of representing these eigenvalues or the components of the eigenvectors in a complex frequency plane, in which the real part of the frequency is represented in the abscissas and the ordinates are used to represent the corresponding imaginary part [36, 57, 58].

In this section we analyze the reflection problems in order to introduce the concept of the zeros and the poles of the reflection coefficient representing the scattering of the problem, in the complex frequency plane. The information given by this representation will be exploited to interpret the PA in terms of the critical coupling conditions.

Consider the simple case of a slot with a quarter wavelength resonance plugged to a waveguide as shown in Figure 2(a). Since the interest is in the low frequency regime, only single-mode reflected waves are considered. In other words, attention is paid to the range of frequencies, f, smaller than the cutoff frequency of the waveguide; therefore the problem can be considered as 1D. This one-mode approximation allows us to illustrate with very simple analytic expressions the appearance of the zeros and poles of the reflection coefficient. The geometry of interest is displayed in Figure 2(a): it corresponds both to an incident wave on a slot of length L and section S_2 at the end of a waveguide of section S_1 or to a wave normally incident on a wall with periodic slots.

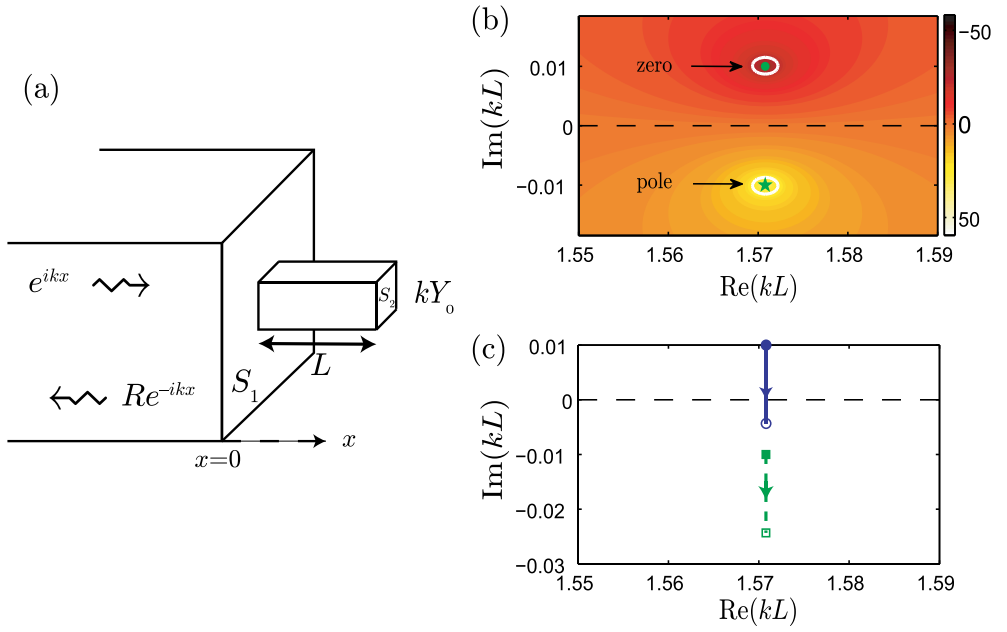

Figure 2. Analysis of the complex plane for the slot. (a) Scheme of the slot. (b) Representation of the 20 log(|R|) in the complex frequency plane for the lossless case. The analyzed slot has the following parameters $L = 25$ cm, $S_2/S_1 = 0.1$. The dot and the star represent the zero and the pole respectively obtained considering the low frequency approximation (Equations (6) and (7)). (c) Dependence of the complex frequency of the zero (continuous line) and the pole (dashed line) on the losses added to the system. Arrows show the direction of the trajectory of the pole as the losses are increased. Filled symbols represent the lossless case and open symbols represent the last considered lossy case.

A plane wave is incident from the left such that a total wave of the form

$$p = \mathrm{e}^{\mathrm{i}kx} + R\mathrm{e}^{-\mathrm{i}kx} \tag{4}$$

is created in $x < 0$. The wavenumber is $k = \omega/c$ with c the acoustic wave speed.

2.2.1. *Lossless case*

For a rigid wall at the end of the slot $p'(L) = 0$ and thus $p'(0^+)/p(0^+) = k\tan(kL)$, with the prime denoting differentiation with respect to x. Then, assuming a one-mode approximation, the continuity conditions are $p(0^-) = p(0^+)$ and $S_1 p'(0^-) = S_2 p'(0+)$. That leads to the expression of the reflection coefficient

$$R = \frac{\cot(kL) + \mathrm{i}S_2/S_1}{\cot(kL) - \mathrm{i}S_2/S_1}. \tag{5}$$

For a real frequency (k real), $|R| = 1$ is recognized as dictated by energy conservation. Going to the complex frequency plane (complex k), Equation (5) shows that R satisfies $\overline{R(k)} = 1/R(\overline{k})$ where $\overline{r(k)}$ and $\overline{k}$ represent the complex conjugate of $R(k)$ and k respectively. The reflection coefficient has pairs of poles and zeros that are complex conjugate, where the poles have a negative imaginary part and the zeros have a positive imaginary part. These properties are general [59]; they come from the structure of the wave equation (Helmholtz equation) and are independent of the one-mode approximation used in this calculation.

From (5), the poles correspond to $\cot(kL) - \mathrm{i}S_2/S_1 = 0$ and the zeros to $\cot(kL) + \mathrm{i}S_2/S_1 = 0$. Assuming that the slot is thin ($S_2/S_1 \ll 1$), the expression of the first pole–zero pair is given by

$$(kL)_{\text{pole}} = \frac{\pi}{2} - \mathrm{i}\frac{S_2}{S_1}, \tag{6}$$

$$(kL)_{\text{zero}} = \frac{\pi}{2} + \mathrm{i}\frac{S_2}{S_1}. \tag{7}$$

Next pairs of pole–zero are just shifted by $m\pi$ ($m \geq 1$) and will not be regarded in the following. The complex pole of (6) corresponds to a complex resonance frequency of the slot with an open end at $x = 0$. The imaginary part (S_2/S_1) represents the leakage due to the radiation at the open end towards the exterior of the slot. With the convention of time dependence used in this work, the wave at the resonance frequency decreases as $\mathrm{e}^{\mathrm{Im}(\omega^{\text{pole}})t}$ (where $\omega^{\text{pole}} = (kL)_{\text{pole}}c/L$), thus the decay time, τ_{leak}, can be related with the quality factor due to the leakage as,

$$Q_{\text{leak}} = \frac{\mathrm{Re}(\omega_{\text{pole}})\tau_{\text{leak}}}{2} = \frac{\mathrm{Re}(\omega_{\text{pole}})}{2\mathrm{Im}(\omega_{\text{pole}})}, \tag{8}$$

where the leakage rate can be defined as $\Gamma_{\text{leak}} = 1/\tau_{\text{leak}} = \mathrm{Im}(\omega_{\text{pole}})$. The $|R|$ in the complex frequency plane is shown in Figure 2(b). According to the theory, there is a pole with negative imaginary part and a zero which is its complex conjugate (with an opposite imaginary part). In the neighborhood of the pole–zero pair, R is just given by $R = (kL - \pi/2 - \mathrm{i}S_2/S_1)/(kL - \pi/2 + \mathrm{i}S_2/S_1)$. Consequently, for real frequency (k real), although $|R| = 1$, the complex resonance frequency is seen as a rapid phase change of the reflection coefficient around $kL = \pi/2$. The imaginary part, which is related with the leakage rate of energy from the slot to the surrounding space, is equal to S_2/S_1, and it gives the quality factor of this rapid phase change.

2.2.2. *Lossy case*

Now a lossy coating at the end of the slot, such that $p'(L) = kY_0p(L)$ where $\mathrm{Im}(Y_0) > 0$ is considered. The reduced admittance Y_0 has a positive imaginary part that corresponds to the loss of the coating. By using $p'(0^+)/p(0^+) = (k\tan(kL) + p'(L)/p(L))(1 - \tan(kL)/k \times p'(L)/p(L))$, the reflection coefficient is changed from (5) to

$$R = \frac{\cot(kL) - Y_0 + \mathrm{i}S_2/S_1(1 + Y_0\cot(kL))}{\cot(kL) - Y_0 - \mathrm{i}S_2/S_1(1 + Y_0\cot(kL))}. \tag{9}$$

Due to the loss ($\mathrm{Im}(Y_0) > 0$), $|R| < 1$ for real frequency k. Besides, the pole–zero pair is now shifted in the complex k plane. For thin slot and small coating ($Y_0 = O(S_2/S_1) \ll 1$), the pair is given analytically by

$$(kL)_{\text{pole}} = \frac{\pi}{2} - \mathrm{i}\frac{S_2}{S_1} - Y_0, \tag{10}$$

$$(kL)_{\text{zero}} = \frac{\pi}{2} + \mathrm{i}\frac{S_2}{S_1} - Y_0. \tag{11}$$

By comparing (6)–(7) and (10)–(11) the effect of the lossy coating is explicit: the pole and the zero are shifted downwards in the complex frequency plane by Y_0. This shift is illustrated in Figure 2(c) for a purely resistive admittance $Y_0 = \mathrm{i}A$ with $A > 0$.

From the point of view of absorption defined as $\alpha = 1 - |R|^2$, all that has decisive consequences: the zero of r coincides with the real frequency axis (k real) of the complex plane when

$$S_2/S_1 = \mathrm{Im}(Y_0). \tag{12}$$

Then, there is total absorption (for a real frequency) and it corresponds to the critical coupling where the leakage (S_2/S_1) is balanced by the loss ($\mathrm{Im}(Y_0)$). It is worthwhile to emphasize here that the narrowband or broadband character of this absorption peak is only governed by the radiation

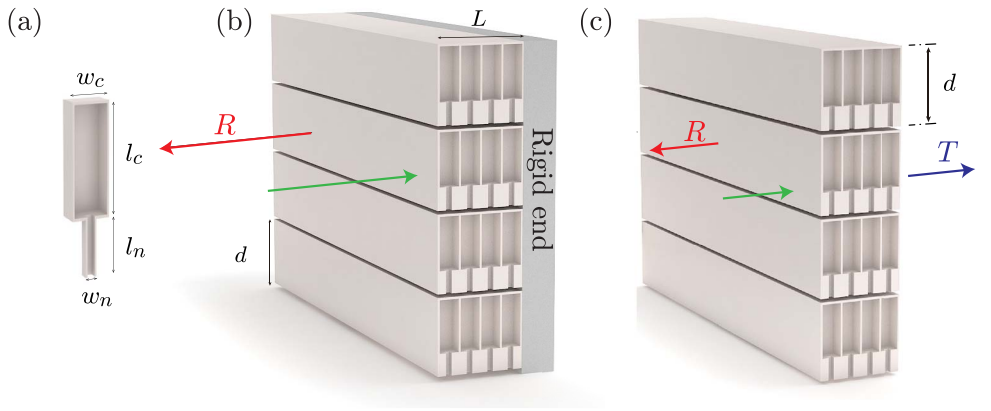

Figure 3. (a) Square cross-section HRs. (b) Conceptual view of the metamaterial panel placed on a rigid end with $N = 4$ layers of HRs. (c) Conceptual view of the metamaterial panel with $N = 4$ layers of HRs for the transmission problem.

leakage through the distance between the pole and the zero in the complex frequency plane. The loss just shifts the pole–zero pair (see (10)–(11)).

The situation of PA in the reflection problem in acoustics, described in this section with a toy model, has been exploited in real conditions to obtain deep sub-wavelength anechoic terminations by means of resonant building blocks made of slow sound metamaterials [32, 37], porous membranes [28], membranes [31], decorated membranes [29], bubble metascreens [33] and aerogel-like metamaterials [34], among other systems.

2.3. *Helmholtz resonators*

In this work we use HRs with either square or cylindrical cross-section. HRs with square (cylindrical) cross sections are characterized by a neck and cavity of width w_n and w_c (of radius r_n and r_c) and length l_n and l_c respectively (see Figure 3(a)). The HR is loaded in cylindrical waveguides (of radius r) or in two-dimensional slits (of height h). Two examples of HRs loaded in slits embedded in panels are shown in Figures 3(b) and (c) for the reflection and transmission problems. The visco-thermal losses in the system are considered in the resonators as well as in the slits or in the main waveguides by using its effective complex and frequency dependent parameters [60].

Using the effective parameters for the neck and cavity elements of a HR, the impedance can be written as

$$Z_{\mathrm{HR}} = \mathrm{i} Z_n \frac{A - \tan k_n l_n \tan k_c l_c}{A \tan k_n l_n + \tan k_c l_c}, \tag{13}$$

with $A = Z_c/Z_n$, l_n and l_c are the neck and cavity lengths, S_n and S_c are the neck and cavity surfaces and k_n and k_c, and Z_n and Z_c are the effective wavenumbers and effective characteristic impedance in the neck and cavity respectively. As we are using either square or cylindrical cross section HRs, the neck and cavity surfaces should be calculated corresponding to each case.

Equation (13) is not exact as long as correction due to the radiation should be included. The characteristic impedance accounting for the neck radiation can be expressed as [61]:

$$Z_{\mathrm{HR}} = -\mathrm{i} \frac{\cos(k_n l_n)\cos(k_c l_c) - Z_n k_n \Delta l \cos(k_n l_n)\sin(k_c l_c)/Z_c - Z_n \sin(k_n l_n)\sin(k_c l_c)/Z_c}{\sin(k_n l_n)\cos(k_c l_c)/Z_n - k_n \Delta l \sin(k_n l_n)\sin(k_c l_c)/Z_c + \cos(k_n l_n)\sin(k_c l_c)/Z_c}, \tag{14}$$

where the correction length is deduced from the addition of two correction lengths $\Delta l = \Delta l_1 + \Delta l_2$ as

$$\Delta l_1 = 0.82\left[1 - 1.35\frac{r_n}{r_c} + 0.31\left(\frac{r_n}{r_c}\right)^3\right] r_n, \tag{15}$$

$$\Delta l_2 = 0.82\left[1 - 0.235\frac{r_n}{r_s} - 1.32\left(\frac{r_n}{r_t}\right)^2\right. \tag{16}$$

$$\left. + 1.54\left(\frac{r_n}{r_t}\right)^3 - 0.86\left(\frac{r_n}{r_t}\right)^4\right] r_n. \tag{17}$$

The first length correction, Δl_1, is due to pressure radiation at the discontinuity from the neck duct to the cavity of the HR [62], while the second Δl_2 comes from the radiation at the discontinuity from the neck to the principal waveguide [63]. This correction only depends on the geometries of the waveguides (or slits), so it becomes important when the duct length is comparable to the radius, i.e., for small neck lengths and for frequencies where $kr_n \ll 1$.

2.4. *Transfer matrix method*

In this work we use the transfer matrix method (TMM) to analyze the wave propagation in the proposed systems. This method allows us to develop discrete models accounting for the finite number of resonators. The transfer matrix is written as:

$$\begin{pmatrix} P_\mathrm{i} \\ U_\mathrm{i} \end{pmatrix} = \mathbf{T}\begin{pmatrix} P_\mathrm{o} \\ U_\mathrm{o} \end{pmatrix}, \tag{18}$$

where P_i and P_o (U_i and U_o) are the incident and the output pressures (velocities) of the system. If the system is made of N resonators, as shown in Figure 3(c) for a single slit, the system can be represented by the following transmission matrix

$$\mathbf{T} = \begin{pmatrix} T_{11} & T_{12} \\ T_{21} & T_{22} \end{pmatrix} = \prod_{n=1}^{N}\left(\mathbf{M}_s\mathbf{M}_\mathrm{HR}^{(n)}\mathbf{M}_s\right).$$

In the case of identical resonators, $\mathbf{M}_\mathrm{HR}^{(n)} = \mathbf{M}_\mathrm{HR}\ \ \forall n$, and then

$$\mathbf{T} = (\mathbf{M}_s\mathbf{M}_\mathrm{HR}\mathbf{M}_s)^N, \tag{19}$$

where the transmission matrix for each lattice step, $\mathbf{M}_s$, is written as

$$\mathbf{M}_s = \begin{pmatrix} \cos\left(k_s\dfrac{a}{2}\right) & \mathrm{i}Z_s\sin\left(k_s\dfrac{a}{2}\right) \\ \dfrac{\mathrm{i}}{Z_s}\sin\left(k_s\dfrac{a}{2}\right) & \cos\left(k_s\dfrac{a}{2}\right) \end{pmatrix}, \tag{20}$$

with κ_s, ρ_s and S_s the effective bulk modulus, density (given by Ref. [60]) and the area of the waveguide where the resonators are loaded respectively. The resonators are introduced as punctual scatterers by a transmission matrix $\mathbf{M}_\mathrm{HR}^{(n)}$ as

$$\mathbf{M}_\mathrm{HR}^{(n)} = \begin{pmatrix} 1 & 0 \\ 1/Z_\mathrm{HR}^{(n)} & 1 \end{pmatrix}. \tag{21}$$

If the system is embedded in a panel of periodic slits with periodicity d, the radiation correction of the slit to the free space should be added to the (19) as

$$\mathbf{M}_{\Delta l_\mathrm{slit}} = \begin{pmatrix} 1 & Z_{\Delta l_\mathrm{slit}} \\ 0 & 1 \end{pmatrix}, \tag{22}$$

with the characteristic radiation impedance $Z_{\Delta l_\mathrm{slit}} = -\mathrm{i}\omega\Delta l_\mathrm{slit}\rho_0/\phi_t S_0$, where S_0 is the area of exterior periodicity, ρ_0 the air density and Δl_slit the proper end correction coming from the

radiation from the slits to the free air. The radiation correction for a periodic distribution of slits can be expressed as [64]:

$$\Delta l_{\text{slit}} = h\phi_t \sum_{n=1}^{\infty} \frac{\sin^2(n\pi\phi_t)}{(n\pi\phi_t)^3}. \tag{23}$$

Note that for $0.1 \leq \phi_t \leq 0.7$ this expression reduces to $\Delta l_{\text{slit}} \approx -\sqrt{2}\ln[\sin(\pi\phi_t/2)]/\pi$. Although (23) is appropriate for a periodic array of slits, it is not exact for slits loading HRs, therefore, we can evaluate a more realistic value for the end correction by reconstructing an equivalent impedance, $\tilde{Z}$, from the reflection coefficient of the zeroth order Bloch mode calculated with the full model and comparing it as [57]:

$$\tilde{Z} - \mathrm{i}Z_e \operatorname{cotan}(k_e L) = -\mathrm{i}\omega \frac{\rho_0}{\phi_t} \Delta l_{\text{slit}}, \tag{24}$$

where Z_e and k_e are the effective acoustic impedance and wave number of the acoustic metamaterial [38]. The end correction using this last approach gives a value that depends on the geometry of the HRs.

Then, in the reflection problem, the reflection coefficient is calculated using the elements of the transfer matrix as

$$R = \frac{T_{11} - Z_0 T_{21}}{T_{11} + Z_0 T_{21}}, \tag{25}$$

with $Z_0 = \rho_0 c_0 / S_0$, and finally the absorption as $\alpha = 1 - |R|^2$.

In the symmetric reciprocal transmission problem, the reflection and the transmission coefficients are calculated as

$$T = \frac{2\mathrm{e}^{-\mathrm{i}kL}}{T_{11} + T_{12}/Z_0 + Z_0 T_{21} + T_{22}}, \tag{26}$$

$$R = \frac{T_{11} + T_{12}/Z_0 - Z_0 T_{21} - T_{22}}{T_{11} + T_{12}/Z_0 + Z_0 T_{21} + T_{22}}. \tag{27}$$

In the antisymmetric reciprocal transmission problem, the reflection and the transmission coefficients are calculated as

$$T = \frac{2\mathrm{e}^{-\mathrm{i}kL}}{T_{11} + T_{12}/Z_0 + Z_0 T_{21} + T_{22}}, \tag{28}$$

$$R^+ = \frac{T_{11} + T_{12}/Z_0 - Z_0 T_{21} - T_{22}}{T_{11} + T_{12}/Z_0 + Z_0 T_{21} + T_{22}}, \tag{29}$$

$$R^- = \frac{-T_{11} + T_{12}/Z_0 - Z_0 T_{21} + T_{22}}{T_{11} + T_{12}/Z_0 + Z_0 T_{21} + T_{22}}. \tag{30}$$

3. Perfect absorption in one port systems (pure reflection problem)

In this section we experimentally and analytically report PA for audible sound, by the mechanism of critical coupling, with a sub-wavelength single resonant scatterer made of a HR with a closed waveguide structure [28]. The controlled balance between the energy leakage of the several resonances and the inherent losses of the system leads PA peaks.

The configurations analyzed in this section can be considered as equivalent to an asymmetric Fabry–Pérot cavity of length L with two different mirrors, i.e., the resonant scatterer, considered as a point-scatterer because it is sub-wavelength, and the rigid backing (as schematically shown in Figure 4(a)). The absorption of this system can be expressed as $\alpha = 1 - |R|^2$, where R is the complex reflection coefficient obtained from the standard three-medium layer Fresnel equation [65],

$$R = R_R + \frac{T_R^2 R_t \mathrm{e}^{\mathrm{i}2kL}}{1 - R_R R_t \mathrm{e}^{\mathrm{i}2kL}}, \tag{31}$$

where R_R and R_t are the reflection coefficients of the resonant element and of the termination, respectively (in our case, $R_t = 1$). Considering inherent losses in this configuration, the PA is

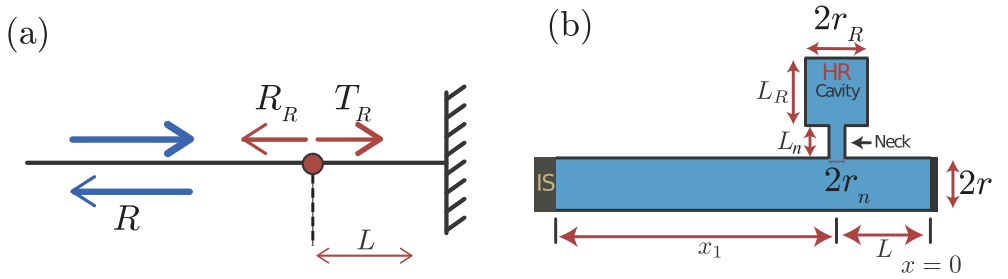

Figure 4. (a) Asymmetric Fabry–Pérot resonator made of a resonant element (red point) and a rigid backing at distance L from the resonator. (b) Shows the resonator set-up. In the set-up an Impedance Sensor (IS) [61] is used for the measurements.

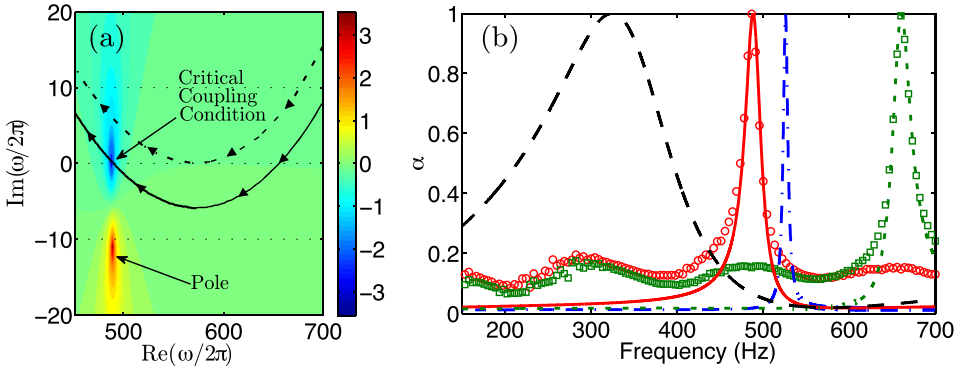

Figure 5. (a) Complex frequency map of $\log|r|$ for the resonant system with $L_R = 8.3$ cm. Black dashed (continuous) line represents the trajectory of the zero of $|r|$ for the lossless (lossy) case in the complex plane increasing L_R (sense of the increasing shown by arrows over the lines). (b) Red continuous and green dotted lines (open red circles and open green squares) represents the absorption coefficient α for the configurations $(L_R, f_{CC}) = (8.3\text{ cm}, 484.5\text{ Hz})$ and $(L_R, f_{CC}) = (3.9\text{ cm}, 647\text{ Hz})$. Blue dash-dotted line represents the absorption coefficient for the configuration $(L_R, f_{CC}) = (7\text{ cm}, 526\text{ Hz})$ with half inherent losses of the experimental case. Black dashed line represents the absorption coefficient for the configuration $(L_R, f_{CC}) = (16\text{ cm}, 330\text{ Hz})$ with 20 times the inherent losses of the experimental case. Figure reproduced from Ref. [28].

fulfilled when the reflection coefficient is zero, i.e., when the superposition of the multiple reflections in the cavity (second term in (31)) destructively interferes with the direct reflection from the resonant element (first term in (31)).

Figure 4(b) shows the set-up used for the system with the HR side-loaded to the closed waveguide. The HR is composed of a neck of length $L_n = 2$ cm with radius $R_n = 1$ cm, a cavity with tunable length, L_R, and radius $R_R = 2.15$ cm. The waveguide has a radius $R = 2.5$ cm and $L = 15$ cm. The viscothermal losses at the walls of the waveguide and of the resonator are characterized by both a complex wave vector and a complex impedance [60, 61, 66].

By changing L_R from 0 to 15 cm, i.e., by changing the resonant frequency of the HR, we study the trajectory of the zero of the reflection coefficient in the complex frequency plane for the lossless case. Figure 5(a) (black dashed line) shows the trajectory of the zero of the reflection coefficient that is produced by a hybridized resonance due to the interaction between the resonance of the HR and the resonance of the backing cavity. As shown by the arrows over

the trajectory, the zero moves to lower real frequencies as L_R increases. The characteristics of the modes, i.e., the resonant frequency and the leakage rate are related to the real and imaginary part of the zero in the complex frequency plane respectively [28].

Now we consider the viscothermal losses in the system and we observe that the trajectory of the zero down-shifts (black continuous line) with respect to the lossless case. The critical coupling condition is satisfied at the frequency, f_{CC} at which the trajectory of the zero crosses the real frequency axis. For the analyzed system, one can clearly see two crossing points, i.e., two different configurations producing PA. These points correspond to $(L_R, f_{\mathrm{CC}}) = (8.3\ \mathrm{cm}, 484.5\ \mathrm{Hz})$ and $(L_R, f_{\mathrm{CC}}) = (3.9\ \mathrm{cm}, 647\ \mathrm{Hz})$. Figure 3(a) shows the reflection coefficient (31) in the complex frequency plane for the configuration $(L_R, f_{\mathrm{CC}}) = (8.3\ \mathrm{cm}, 484.5\ \mathrm{Hz})$. Similarly, a complex map for the configuration $(L_R, f_{\mathrm{CC}}) = (3.9\ \mathrm{cm}, 647\ \mathrm{Hz})$ with the zero in the real frequency axis can also be obtained [28]. We find analytically PA ($\alpha = 1$) for the two above mentioned configurations at 484.5 Hz and 647 Hz as shown in Figure 3(b), in agreement with the crossing points of the trajectory of the zero with the real frequency axis represented in Figure 5(a) (black continuous line). Experiments show also very good agreement with the theoretical predictions, producing 100% of absorption for these configurations at the corresponding frequencies with a relative narrow bandwidth of frequencies due to the small leakage of the resonance.

Generally, by changing the inherent losses of the system, we can move the trajectory of the zero in the complex plane, and we can always find a configuration with the good balance between the energy leakage and the inherent losses of the whole resonator to fulfill the critical coupling condition and activate the PA. In particular, increasing of inherent losses in the system produces two main effects: the critical coupling condition is shifted in frequencies and the PA peak becomes broadband because the critical coupled resonances are more leaky.

In order to show these effects, we theoretically analyze the cases of weak and large inherent losses. Dash-dotted blue line and dashed black line in Figure 5(b) represent the absorption coefficient for the configurations $(L_R, f_{\mathrm{CC}}) = (7\ \mathrm{cm}, 526\ \mathrm{Hz})$ and $(L_R, f_{\mathrm{CC}}) = (16\ \mathrm{cm}, 330\ \mathrm{Hz})$ each one with the right amount of inherent losses to accomplish the critical coupling. The first (second) one corresponds to a situation with 0.5 (20) times the inherent losses of the experimental case. With small amount of inherent losses, one can find a very narrow PA peak while with large amount of inherent losses the PA peak becomes broad. The broad character is due to the large energy leakage of the critically coupled resonance [28].

4. Perfect absorption in two port systems

In this section we review the main features of PA through the interplay of the inherent losses and transparent modes [67–71] with high Q factor as shown in [42]. These modes are generated in a two-port one-dimensional waveguide which is side-loaded by isolated resonators with moderate Q factor. This mode allows transparency in the lossless case, i.e., a perfectly transmitted wave, within a narrow spectral range. These modes are characterized by an extreme dispersion which leads to slow waves. In mirror symmetric structures, we show that in the presence of small inherent losses, these modes lead to coherent PA associated with one-sided absorption slightly larger than 0.5. In asymmetric structures, near perfect one-sided absorption is possible (96%) with a deep sub-wavelength sample ($\lambda/28$).

4.1. *Point symmetric*

A point symmetric scatterer made of two detuned HRs ($f_1^{\mathrm{HR}} \neq f_2^{\mathrm{HR}}$) located at the same axial position is analyzed in this section (see the sketch in Figure 6(b)). We define the detuning parameter as $(f_2^{\mathrm{HR}} - f_1^{\mathrm{HR}})/\Gamma_L$, where $\Gamma_L = 3.14$ Hz is the decay rate due to losses of the HRs [42].

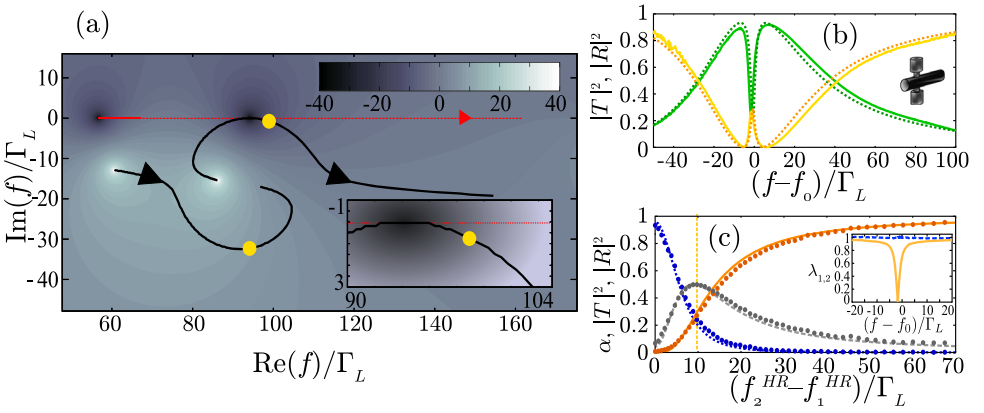

Figure 6. Point symmetric scatterer. (a) Theoretical lossless transmission coefficient (logscale) in the complex frequency plane with the trajectories of the poles (black lines) and of the zero (red dashed line) for $(f_2^{\mathrm{HR}} - f_1^{\mathrm{HR}})/\Gamma_L \in [-37;67]$. The positions of the poles are marked for $(f_2^{\mathrm{HR}} - f_1^{\mathrm{HR}})/\Gamma_L = 9.8$ (yellow dots) and the underlying colormap image corresponds to $(f_2^{\mathrm{HR}} - f_1^{\mathrm{HR}})/\Gamma_L = -37$. Inset: zoom around the critical coupling point. (b) Theoretical with losses (dashed curves), experimental (continuous curves) transmission (yellow curves) and reflection (green curves) coefficients versus frequency for $(f_2^{\mathrm{HR}} - f_1^{\mathrm{HR}})/\Gamma_L = 9.8$ with $f_0 = 311$ Hz. (c) Absorption (gray), transmission (orange) and reflection (blue) coefficients at $f_{\max}$ versus $(f_2^{\mathrm{HR}} - f_1^{\mathrm{HR}})/\Gamma_L$ (curves for theory and dots for experiments). Inset: eigenvalues of the experimental S-matrix for $(f_2^{\mathrm{HR}} - f_1^{\mathrm{HR}})/\Gamma_L = 9.8$.

Ignoring the losses, it has been shown that, for small values of the detuning parameter, the transmission coefficient presents an extraordinary induced transparent (EIT) like mode with unity transmission at $f_0 = (f_2^{\mathrm{HR}} + f_1^{\mathrm{HR}})/2$ [67–71]. The lossless transmission coefficient in the complex frequency plane is displayed in Figure 6(a); this reveals two poles which are hybridized resonances resulting from the two resonances of the HRs. As the detuning parameter changes, in our case by increasing the resonance frequency of one HR while keeping the other one fixed at $f_1^{\mathrm{HR}} = 294$ Hz, the poles move (sense of the arrows in Figure 6(a)), interact and repel each others. As $f_2^{\mathrm{HR}} - f_1^{\mathrm{HR}} \to 0$, one pole at f_{pole}, with $\mathrm{Re}(f_{\mathrm{pole}}) \simeq f_0$, approaches the real axis giving rise to an EIT-like mode with high Q factor. In other words, the interaction of the two resonances leads to a dark mode (the EIT-like mode) and a bright mode (with a corresponding pole far from the real axis).

We now analyze the experimental results and compare them with the theoretical predictions taking into account the losses [42] by looking at the scattering coefficients as a function of the frequency (corresponding to the real axis in the complex frequency plane). For small detuning parameter, the viscothermal losses importantly reduce the amplitude of the transparent peak associated with the EIT like mode: instead of the unity transmission in the lossless case, the peak can take values between 0 and 1. For each value of the detuning parameter, the transparent peak is associated with a peak of absorption found at $f_{\max}$ (slightly different from f_0 due to the losses). The maximum peak of absorption is found with $(f_2^{\mathrm{HR}} - f_1^{\mathrm{HR}})/\Gamma_L = 9.8$, highlighted with circles in Figure 6(a), at $f_{\max} = 306$ Hz. The relevant scattering coefficients are displayed in Figure 6(b). According to the theoretical considerations on point symmetric scatterers, $|T(f_{\max})| = |R(f_{\max})| = 0.5$ corresponds to $\alpha_s(f_{\max}) = 1$ and consequently to $\alpha(f_{\max}) = 0.5$. This one-sided incident wave maximum of absorption is found when the leakage of the EIT-like mode is tuned in order to balance the inherent losses, i.e., it is critically coupled [33, 42, 52, 72]. This is confirmed in

Figure 6(c) where the scattering coefficients and the absorption at $f_{\max}$ are plotted as a function of the detuning parameter. In addition, one experimental eigenvalue becomes zero at $f_{\max}$ as shown in Figure 6(c). As mentioned above, this is the symmetrical CPA [56]; the case at which the incident waves from the two sides of the sample, corresponding to the S-matrix eigenvector such as $v_2/v_1 = 1$, are completely absorbed.

4.2. *Mirror symmetric resonators*

We now pay attention to mirror symmetric scatterers. The interest of these scatterers, compared to the point symmetric scatterers, relies on the fact that the one-sided absorption α takes value larger than 0.5. This happens since α_a can be different from zero. Two tuned HRs ($f_1^{\mathrm{HR}} = f_2^{\mathrm{HR}} = f^{\mathrm{HR}}$) located at different axial positions and separated by the distance l forms the mirror symmetric resonator analyzed in this section (see the sketch in Figure 7(a)). Now, the detuning parameter is defined as $k^{\mathrm{HR}}l = 2\pi f^{\mathrm{HR}}l/c_0$ where c_0 is the sound velocity. As in the point symmetric scatterer case, we first inspect the behavior of the lossless transmission coefficient in the complex frequency plane. In addition to the two HR-related poles, multiple poles due to the Fabry–Pérot resonances of the waveguide appear. Once the resonance frequency of the HRs is close to a Fabry–Pérot frequency f^{FP} ($k^{\mathrm{HR}}l \sim n\pi$, where $n \in \mathbb{N}$ including $n = 0$), one of the poles approaches the real axis and gives rise to an EIT-like mode. In Figure 7(a), the case where $k^{\mathrm{HR}}l \to \pi$ is shown. As before, the viscothermal losses can subsequently reduce the amplitude of the transparent peak associated to the EIT-like mode, see Figures 7(b) and (c). The discrepancies between experimental results and theoretical predictions, larger than in the case of point symmetric scatterers, are attributed to a larger leakage outside the waveguide and to the difficulty to get $f_1^{\mathrm{HR}} = f_2^{\mathrm{HR}}$ in experiments. We continue our analysis by studying some particular detuning parameters values. For instance, we experimentally (theoretically) find that $R(f_{\mathrm{CPA}}) \simeq -T(f_{\mathrm{CPA}})$ for $k^{\mathrm{HR}}l/\pi = 0.82$ and 1.17 ($k^{\mathrm{HR}}l/\pi = 0.86$ and 1.14) at f_{CPA}.

According to the theory, these cases correspond to $\alpha_s(f_{\mathrm{CPA}}) = 1$, which is equivalent to a symmetrical CPA point, $\lambda_1(f_{\mathrm{CPA}}) = 0$. In Figure 7(b), we verify the existence of a symmetrical CPA point by plotting the scattering coefficients, as well as the eigenvalues of the experimental S-matrix, as a function of frequency for $k^{\mathrm{HR}}l/\pi = 1.17$. Importantly, at these detuning parameter values, both in theory and experiments, the one-sided absorption α takes a value larger than 0.5 around f_{CPA}. Indeed, as we mentioned above $\alpha_a \neq 0$, which is confirmed experimentally by the fact that $\lambda_2 \neq 1$, see inset of Figure 7(b). It is worth to comment here that, by using HRs of smaller Q factor, we observe a larger value of α. Overall, we find that the maximum peak of absorption is $\alpha(f_{\max}) = 0.55$ in theory ($\alpha(f_{\max}) = 0.6$ in experiments) for $k^{\mathrm{HR}}l/\pi = 0.86$ and 1.14 as shown in Figure 7(c); as before, we show that this corresponds to the critical coupling of the relevant EIT-like mode [42]. The maximum peak of absorption appears theoretically at the symmetrical CPA point, i.e., for the same detuning parameter and at $f_{\max} = f_{\mathrm{CPA}}$. This is explained by the experimentally observed nearly constant behavior of λ_2, and thus α_a, which is not the case of asymmetric scatterers as we will see below.

4.3. *Perfect absorption in asymmetric systems*

To enhance the one-side incident wave absorption, let us now turn to the case of asymmetric scatterers. We consider an additional degree of freedom in the setup: two detuned HRs ($f_1^{\mathrm{HR}} \neq f_2^{\mathrm{HR}}$) separated by the distance l (see the sketch in Figure 8(a)). The mirror symmetry is broken ($R^- \neq R^+$) and two detuning parameters are defined as $k_1^{\mathrm{HR}}l$ and $k_2^{\mathrm{HR}}l$. Figure 8(a) shows the maximum of one-sided absorption found at $f_{\max}$, which is defined with the left incoming wave $\alpha^- = 1 - |R^-|^2 - |T|^2$, as a function of the two detuning parameters, where the red dashed line

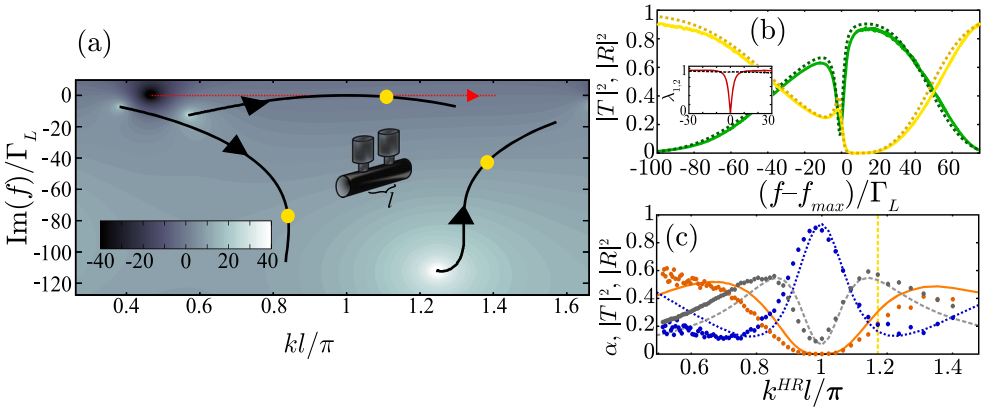

Figure 7. Mirror symmetric scatterer, $l = 30$ cm. (a) Theoretical lossless transmission coefficient (log-scale) in the complex frequency plane with the trajectories of the poles (black lines) and of the zeros (red dashed line) with $k^{\mathrm{HR}}l/\pi \in [0.35; 1.40]$ and $k = 2\pi f/c_0$. The positions of the poles are marked for $k^{\mathrm{HR}}l/\pi = 1.14$ (yellow dots) and the underlying colormap image corresponds to $k^{\mathrm{HR}}l/\pi = 0.35$. (b) Theoretical with losses (dashed curves), experimental (continuous curves) transmission (yellow curves) and reflection (blue curves) coefficients versus frequency for $k^{\mathrm{HR}}l/\pi = 1.17$ with $f_{\mathrm{max}} = 645$ Hz. Inset: eigenvalues of the experimental S-matrix for $k^{\mathrm{HR}}l/\pi = 1.17$. (c) Absorption (gray), transmission (orange) and reflection (blue) coefficients at f_{max} versus $k^{\mathrm{HR}}l$ (curves for theory and dots for experiments).

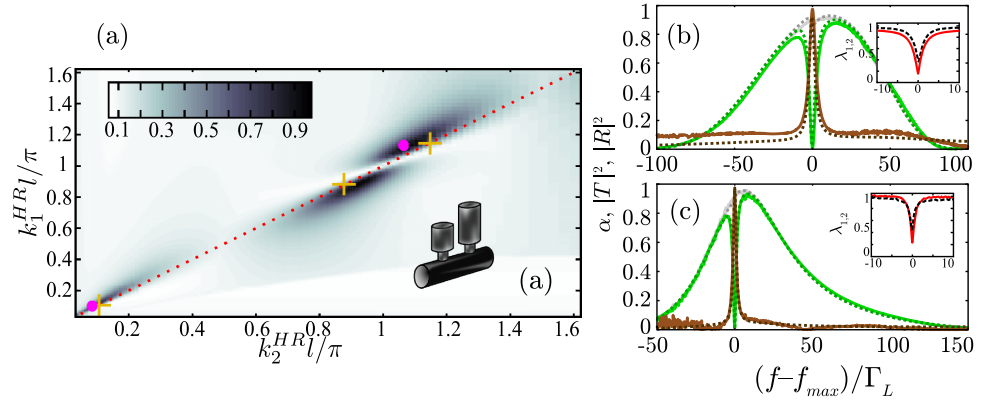

Figure 8. Asymmetric scaterrer. (a) Theoretical absorption versus $k_1^{\mathrm{HR}}l/\pi$ and $k_2^{\mathrm{HR}}l/\pi$. The red dashed line corresponds to the mirror symmetric scatterers. (b)–(c) Theoretical (dashed curves) and experimental (continuous curves) absorption (brown), reflection from left (green) and from right (gray) coefficients. Inset: eigenvalues of the experimental S-matrix. (b) $l = 30$ cm, $k_1^{\mathrm{HR}}l/\pi = 1.14$, $k_2^{\mathrm{HR}}l/\pi = 1.06$ and $f_{\mathrm{max}} = 618$ Hz. (c) $l = 5$ cm, $k_1^{\mathrm{HR}}l/\pi = 7.7.10^{-2}$, $k_2^{\mathrm{HR}}l/\pi = 7.2.10^{-2}$ and $f_{\mathrm{max}} = 244$ Hz.

corresponds to the mirror symmetric scatterer case. Close to the maximum peak of absorption for mirror symmetric scatterers (highlighted by crosses), there exist asymmetric scatterers presenting a Unidirectional Near Perfect One-sided Absorption (UNPOA). Figures 8(b) and (c) show the absorption, the right and left reflection coefficients as a function of frequency for two cases

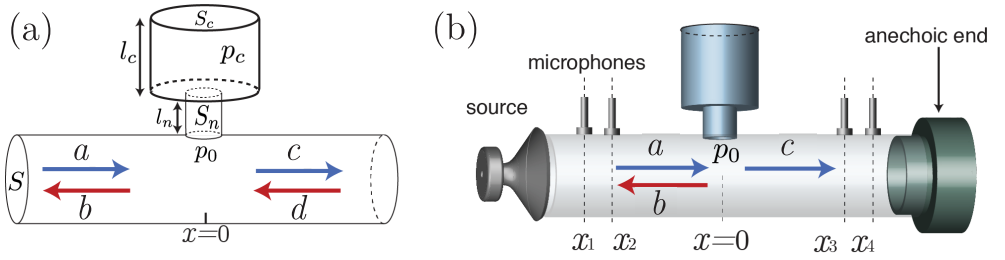

Figure 9. (a) Schematic representation of the system under study: a Helmholtz resonator side-loaded to a cylindrical waveguide. The two-port scattering process is also indicated by the arrows. (b) The experimental setup used for our measurements.

of UNPOA (highlighted by magenta points in Figure 8(a)). Figure 8(b) corresponds to the case where the absorption reaches 0.98 with $k_1^{\mathrm{HR}} l/\pi = 1.14$ and $k_2^{\mathrm{HR}} l/\pi = 1.06$. More interestingly, the absorption is 0.96 for $k_1^{\mathrm{HR}} l/\pi = 0.08$ and $k_2^{\mathrm{HR}} l/\pi = 0.07$ in Figure 8(c). This latter case is particularly appealing because it reveals the possibility of UNPOA with a deep sub-wavelength structure (in the experiment, $f_{\max} = 244$ Hz and $l = 5$ cm corresponding to $\lambda/28$). Note also that $|R^+| > 0.9$ and $R^- \simeq 0$ near $f_{\max}$. This clearly demonstrates the unidirectional character of the absorber. Besides, it is observed that both eigenvalues of the scattering matrix λ_1 and λ_2 go to near zero values at $f_{\max}$ (see insets in Figures 8(b) and (c)). This differs importantly from the eigenvalues observed with the point symmetric and mirror symmetric scatterers where only one of them is going to zero.

4.4. *Nonlinear perfect absorption*

In the previous part, we have shown how the critical coupling condition (and consequently CPA) can be achieved either by tuning the losses of a single scatterer or by tuning the interaction between two different scatterers passively by changing the geometry. We now exploit the possibility that CPA can be induced only by changing the wave amplitude and the effects of nonlinearity. In particular, we study a two-port system composed of a cylindrical waveguide with section S side-loaded at $x = 0$ by a HR. In the case of two high pressure incident waves from each port of the system, we can derive simplified equations describing the dynamics of the system. For sufficiently low frequencies we assume incompressibility of the fluid in the HR's neck and uniform pressure field in its cavity.

By using the linearized mass and momentum conservation laws in the waveguide, continuity of the pressure at $x = 0$, and by considering boundary conditions for CPA (symmetric input waves), the dynamics of the pressure in the cavity of HR $p_c(t)$ side-loaded to the waveguide is found to be [43]

$$\ddot{p}_c + \omega_0^2 p_c + (r_L - \gamma + \beta|\dot{p}_c|)\dot{p}_c = 0. \tag{32}$$

$(.)$ denotes differentiation with respect to time, $\omega_0^2 = c_0^2 S_n / l'_n l_c S_c$ is the resonance frequency of the HR with c_0 the speed of sound. l_c and S_c are respectively the section and the length of the cavity while l'_n denotes the corrected length of the neck (see Figure 9(a)). The viscothermal losses in the resonator are quantified by the small parameter r_L. Finally, β is connected with flow separation and vorticity in the neck and quantifies the nonlinear losses in the HR. $\gamma = c_0^2 S_n / 2 l'_n S$ describes the coupling strength between the HR and the waveguide. The leakage rate of energy out of the HR is described by the additional dissipative term proportional to γ. In this representation, CPA is achieved when the leakage term analogous to $\dot{p}_c(t)$ (energy going away from the resonator) is vanishing. In consequence, we directly observe that, in the linear regime, the critical coupling

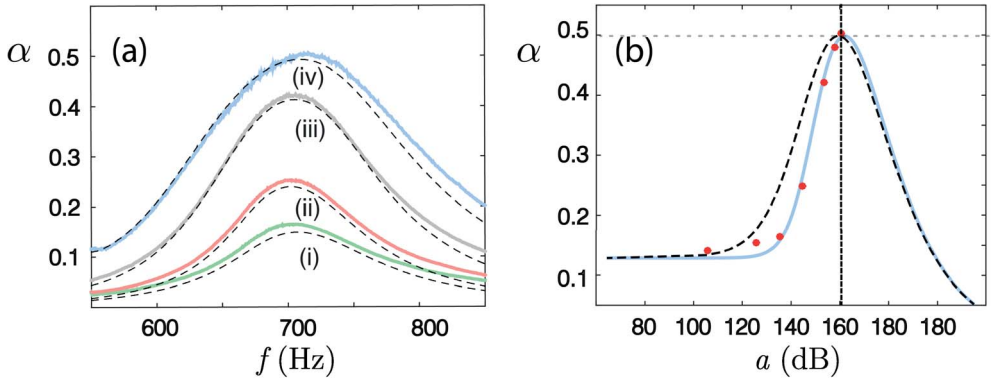

Figure 10. (a) Absorption as a function of frequency for different incident amplitudes $|a|$. Solid lines depict the measured absorption and dashed lines illustrate analytical results. (b) Absorption at the frequency $f_0' = 710$ Hz as a function of the amplitude of the incident wave $|a|$. Blue solid (dashed) line corresponds to the nonlinear impedance model using the fitting parameter $\Delta = 0.15$ ($\Delta = 0$). Dots indicate the corresponding experimental measurements. The vertical dashed line depicts the prediction of (33) for the CPA condition.

condition $r_L = \gamma$ is recovered. On the other hand, it can be found that the combined effects of the presence of losses and nonlinearity can be used to reach the critical coupling condition i.e.

$$\frac{4}{3\pi}\frac{|u_n|}{l_n} + r_L = \gamma, \tag{33}$$

where u_n is the acoustic particle velocity in the HR's neck. To obtain the last equation, a perturbation technique [26] up to first order, neglecting the contribution of higher harmonics is used, assuming a weak nonlinearity. Note that this particular nonlinearity does not introduce a frequency shift of the resonance. We perform one-sided incidence experiments (see Figure 9(b)) to confirm the nonlinear critical coupling by measuring the absorption for different amplitudes and frequencies of incident waves a. We want to verify that nonlinear losses can lead to an absorption $\alpha = 0.5$ (as in any two-port system with one-sided incident wave, see Section 2) when condition (33) is satisfied. To do so we use the 4 microphones method to measure the reflectance and the transmittance of the system and deduce the absorption (see Figure 9(b)).

The panel (a) of Figure 10 shows the absorption as a function of frequency where the solid lines depict the measured absorption for different incident wave amplitudes. We observe that by increasing the incident wave amplitudes $|a|$, the maximum of absorption increases and reaches the value of $\alpha = 0.5$ when $|a| = 160$ dB at the resonance frequency $f_0' = 710$ Hz. The dashed lines in Figure 10(a) show the theoretical predictions as obtained using the nonlinear impedance

$$Z_{HR}^{NL} = Z_{HR}^{L} + \frac{1}{1+\Delta St}\frac{4\rho_0|u_n|}{3\pi S_n C_{vc}^2},$$

where Z_{HR}^{L} is the linear impedance of the HRs (given by (14)), C_{vc}^2 is the vena-contracta coefficient having a value of ≈ 0.7 for a neck with hard edges and St is the Strouhal number. The fitting parameter Δ is chosen to take the value 0.15 and the velocity of the neck is calculated using the experimental values of the incident pressure. The theory and experiments are in good agreement demonstrating that the nonlinear response of the HR is adequately described by the nonlinear impedance.

To further illustrate the fact that the incident wave amplitude can be employed as a tuning parameter to obtain CPA, we show, in Figure 10(b), the absorption for the resonance frequency

f_0' as a function of incident amplitude wave $|a|$. The (red) dots depict the experimental values showing that $\alpha = 0.5$ is reached for $|a| = 160$ dB. This value is predicted by the (33) as indicated by the vertical dashed line and this verifies that critical coupling can be induced by nonlinear losses in addition of the linear ones. The blue and dashed lines are obtained using the theoretical nonlinear HR impedance with $\Delta = 0.15$ and $\Delta = 0$ respectively.

5. Perfect absorption in three-port systems

We now proceed by generalizing the results of the previous Section to a more complex structure, i.e., a 3-port system. In particular using (sub-wavelength) HRs, we theoretically and experimentally illustrate an acoustic perfect absorbing 3-port that operates at different frequencies and different intensities as well as relative phases of the input waves. The system under consideration is composed of three identical waveguides connected by a Y-shape connection. Each waveguide is side-loaded by an identical HR, with resonance frequency f_0, placed at the same distance d from the center of the device (Figure 11(b)–(c)).

5.1. *Scattering properties and CPA*

The 3-port acoustic system is reciprocal and symmetric and the corresponding scattering matrix is given by the following equation [53]

$$\begin{pmatrix} b \\ c \\ f \end{pmatrix} = \begin{pmatrix} R & T & T \\ T & R & T \\ T & T & R \end{pmatrix} \begin{pmatrix} a \\ d \\ g \end{pmatrix} = S \begin{pmatrix} a \\ d \\ g \end{pmatrix}, \tag{34}$$

where the frequency dependent coefficients R and T, correspond to the reflection and transmission when only one port is excited. Note that the definition of the S-matrix in (34) with the reflection coefficient in the diagonal is different from the one given in (1). The S-matrix is a *symmetric circulant* matrix due to the geometric symmetry of the 3-port and to the fact that we consider a reciprocal system. The matrix is symmetric due to reciprocity. An important property of the circulant matrix, is that its eigenvectors always remain the same and thus are independent of both the physical system (particular form of R and T) and the frequency. The vectors $(a,d,g)^T \equiv |\psi_{\text{in}}\rangle$ and $(b,c,f)^T \equiv |\psi_{\text{out}}\rangle$ describe the incoming and outgoing waves respectively as shown in Figure 11(a).

The eigenvalue problem associated to the scattering matrix is the following

$$\det(S - \lambda I) = 0, \tag{35}$$

where the eigenvalues are

$$\lambda_0 = R + 2T, \quad \text{and} \quad \lambda_1 = \lambda_2 = R - T, \tag{36}$$

and the corresponding orthonormal eigenvectors are given by

$$\begin{aligned} |u_0\rangle &= \tfrac{1}{\sqrt{3}}(1,1,1)^T, \\ |u_1\rangle &= \tfrac{1}{\sqrt{3}}(1, \mathrm{e}^{2\mathrm{i}\pi/3}, \mathrm{e}^{-2\mathrm{i}\pi/3})^T, \\ |u_2\rangle &= \tfrac{1}{\sqrt{3}}(1, \mathrm{e}^{-2\mathrm{i}\pi/3}, \mathrm{e}^{2\mathrm{i}\pi/3})^T. \end{aligned} \tag{37}$$

To quantify absorption, we use the parameter Θ defined as the ratio of total output to input power

$$\Theta = \frac{|b|^2 + |c|^2 + |f|^2}{|a|^2 + |d|^2 + |g|^2} = \frac{\sum_i \lambda_{i-1}^2 |c_{i-1}|^2}{\sum_i |c_{i-1}|^2} \quad i = 1,2,3, \tag{38}$$

where we use the fact that any input vector can be written as a sum of $|u_i\rangle$, i.e. $|\psi_{\text{in}}\rangle = \sum_i c_i |u_i\rangle$. By definition, CPA occurs when $\Theta = 0$ i.e. no output.

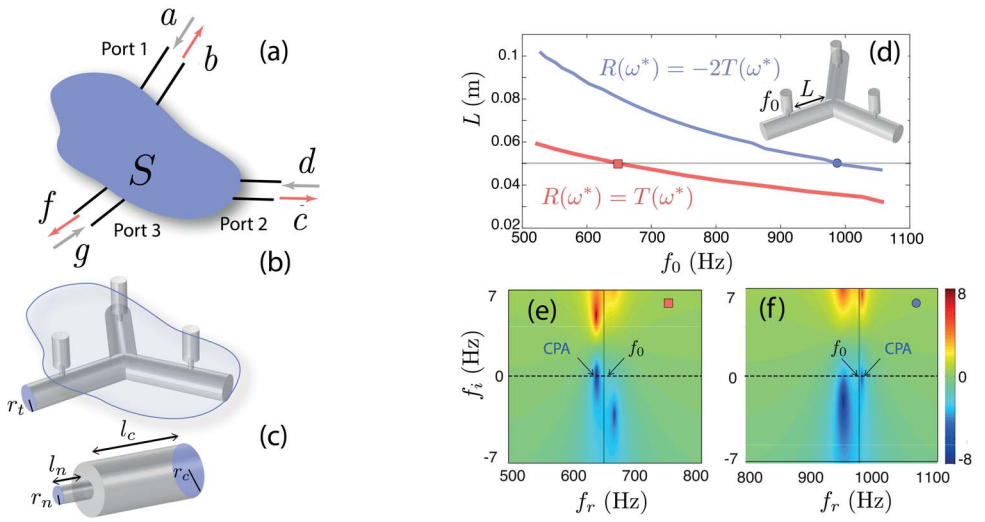

Figure 11. (a) A schematic illustration of a general three port system with incoming and outgoing waves at each port. The scattering matrix S of the system is assumed to be symmetric, at some frequency range, even if the geometry of the device may be not. (b) The symmetric network studied here (not in scale), which is composed by 3 identical cylindrical waveguides with radius $r_t = 2.5 \times 10^{-2}$ m, assembled by a Y-shape connection sideloaded with HRs at a distance d. (c) Details of the HRs composed by a neck with length $\ell_n = 2 \times 10^{-2}$ m, a radius $r_n = 0.45 \times 10^{-2}$ m branched to a cylindrical cavity with radius $r_c = 1.5 \times 10^{-2}$ m and varying length ℓ_c which is used in order to tune the resonance frequency f_0. (d) The upper (lower) curve depicts the symmetric (asymmetric) CPA solutions for varying resonant frequency f_0 and distance d. The horizontal line corresponds to the configurations with $L = 0.05$ m. (e), (f) The determinant $|\det(S)|$ in the complex frequency plane for the configurations corresponding to the two cases of panel (d) with a (red) square and a (blue) circle respectively.

A 3-port network exhibits CPA when the eigenvalues of its S-matrix given by (36) become zero at some particular frequency f^*. Requiring $\lambda_0 = 0$ leads to the following condition on the scattering coefficients $R = -2R \equiv R_s$ associated to a symmetric input of the form $|u_0\rangle$ (Equation (37)) which is completely absorbed (symmetric CPA). The zero value of the degenerate eigenvalues $\lambda_{1,2}$ gives a different CPA condition $R = T \equiv R_a$ with an input wave corresponding to the asymmetric vectors $|u_1\rangle$ or $|u_2\rangle$. In addition, any input in the form $|\psi_{\text{in}}\rangle = A|u_1\rangle + B|u_2\rangle$ will also be completely absorbed (asymmetric CPA).

To achieve CPA, the transmission and reflection coefficients have to be specifically tuned to fulfill the aforementioned CPA conditions. Due to the presence of HRs sided loaded to the waveguide, the strong interference around the resonance frequency greatly modifies both the transmission and the reflection coefficients and allows us to satisfy the CPA conditions. To treat the problem analytically, we assume that for sufficiently low frequencies, only the plane mode is considered in the waveguide and the HRs can be described as point scatterers. In this case, R and T are analytically obtained using the transfer matrix method and are given as a function of f_0 and L.

The CPA conditions are displayed in the parametric space (f_0, L) using the analytical expressions of R and T as shown in Figure 11(d) where the red (lower) curve corresponds to the

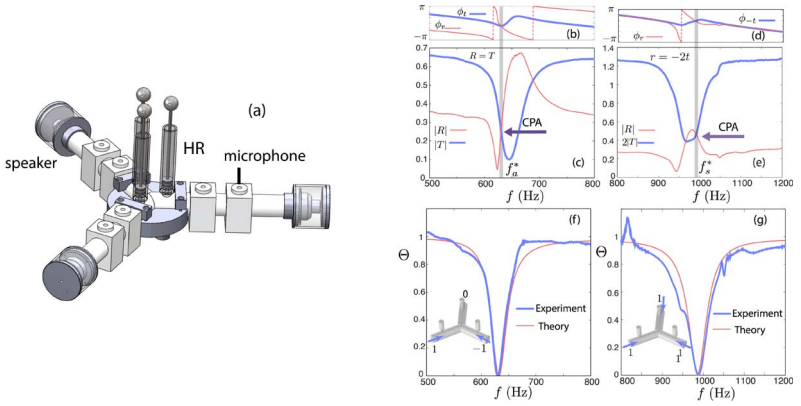

Figure 12. (a) View of the experimental device. (b)–(c) The phase and absolute value of the experimentally measured reflection and transmission coefficients T and R, as a function of frequency, for the configuration which exhibits an asymmetric CPA at $f_a^* = 630$ Hz. The resonance frequency of the HRs is $f_0 = 645$ Hz corresponding to a cavity length $l_c = 0.02$ m. CPA is ensured since both the real and the imaginary parts of r and t are equal for this frequency (vertical gray line). (d)–(e) The phase and absolute value of the experimentally measured reflection and transmission coefficients R and $-2T$, as a function of frequency, for the configuration which exhibits a symmetric CPA at $f_s^* = 988$ Hz. The resonance frequency of the HRs is $f_0 = 975$ Hz corresponding to a cavity length $l_c = 0.89 \times 10^{-2}$ m. CPA appears when the two the curves of both the real and imaginary part become equal, indicated by the vertical gray line. (f)–(g) The output to input power ratio Θ as a function of frequency for the asymmetric and the symmetric CPA respectively. The thick (thin) line corresponds to the experimental (theoretical) measurement. The insets depict the eigenvector used in order to obtain the curves in each case.

asymmetric and the blue (upper) line depicts the symmetric CPA. The occurence of the CPA can also be illustrated in another way; through the complex frequency plane of the determinant of the S-matrix. By scanning the space (f_0, L), the zeros of the determinant move and cross the real axis when CPA occurs fixing the geometry of the system. This is illustrated in Figure 11(e)–(f) where two different configurations, symmetric and asymmetric CPA, are shown respectively. Note that the operating frequency f^* for the CPA is close but not the same as f_0 due to the interaction of the resonances through the waveguides.

5.2. *Experimental demonstration of CPA*

We now experimentally study the scattering of the 3-port network to verify the analytical results of Figure 11(d) with $L = 0.05$ m. The experimental device is illustrated in Figure 12(a). The reflexion and transmission coefficients are determined using a pair of microphones connected to each branch allowing the measurement of the forward and backward waves in each waveguide. With the help of the definition of scattering matrix, the measured incoming and outgoing waves give R and T. Two sets of HRs with different resonance frequencies f_0 are used corresponding to asymmetric and symmetric CPA configurations as indicated respectively by the square and the circle in Figure 11(d). The asymmetric CPA is illustrated in Figure 12(b)–(c) where the CPA condition $R = T$ is fulfilled for $f_a^* = 630$ Hz as indicated by the vertical gray lines. The configuration corresponding to the symmetric case is shown in Figure 12(d)–(e) and the required condition is achieved for $f_s^* = 988$ Hz (vertical gray line).

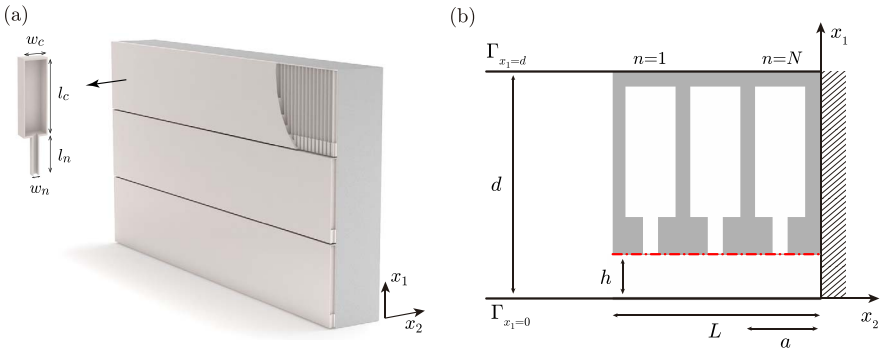

Figure 13. (a) Conceptual view of the thin panel placed on a rigid wall with one layer of square cross-section HRs, $N = 1$. (b) Scheme of the unit cell of the panel composed of a set of N HRs. Symmetry boundary conditions are applied at boundaries $\Gamma_{x_1=d}$ and $\Gamma_{x_1=0}$.

The measurement of r and t allows to experimentally determine the scattering matrix of the 3-port for the two different configurations and for the frequency range of interest. Then the ability of the network to completely absorb an incoming wave can be quantified by considering an input vector $(a,d,g)^T = (1,-1,0)^T$ (inset of Figure 12(f)) and the experimental scattering matrix. With the corresponding output, we determine Θ as shown in Figure 12(f) with the thick solid line, where at the CPA frequency f_a^*, an almost PA is obtained with $\Theta \approx 5\times10^{-4}$. The same analysis is performed for the symmetric CPA, considering $(a,d,g)^T = (1,1,1)^T$ (inset of Figure 12(g)). The result on Θ is shown with the thick solid line in Figure 12(g) where the system reaches a value of $\Theta \approx 10^{-3}$ at f_s^*.

6. Perfect absorption from panels in reflection

In this section we theoretically and experimentally report a perfect and omnidirectional absorbing metamaterial panel with deep sub-wavelength thickness by using the concepts of slow sound and critical coupling [37]. As shown in Figure 13, the system consists of a thin panel perforated with a periodic arrangement of slits, of thickness h, with periodicity d along the x_1 direction. The upper wall of the slit is loaded by N identical HRs arranged in a square array of side a. The HRs, of square cross-section, are characterized by a neck and a cavity widths w_n and w_c, and lengths l_n and l_c respectively. The presence of the HRs introduces a strong dispersion in the slit producing slow propagation, in such a way that the resonance of the slit is down shifted: the slit becomes a deep sub-wavelength resonator. The visco-thermal losses in the system are considered in both the resonators and in the slit by using effective complex and frequency dependent parameters [60] as described in Section 2.3. Therefore, by modifying the geometry, the intrinsic losses of the system can be efficiently tuned and the critical coupling condition can be fulfilled to solve the impedance matching to the exterior medium.

We start by analyzing the dispersion properties inside the slit in order to inspect the slow sound behavior. Periodic boundary conditions are assumed at boundaries $\Gamma_{x_1=0}$ and $\Gamma_{x_1=d}$. At this stage we have to notice that several theoretical models are used to analyze the structure: an approach based on the TMM and the finite element method (FEM) (see Ref. [37] for more details of the models). Figure 14(a) shows the real part of the phase velocity in the slit, calculated both in the lossless and lossy cases, for a metamaterial with parameters $h = 1.2$ mm, $a = 1.2$ cm, $w_n = a/6$, $w_c = a/2$, $d = 7$ cm, $l_n = d/3$, and $l_c = d - h - l_n$. Figure 14(b) shows the corresponding dispersion relation, where a band gap can be observed above the resonant frequency of the HRs, f_{HR}. Due to

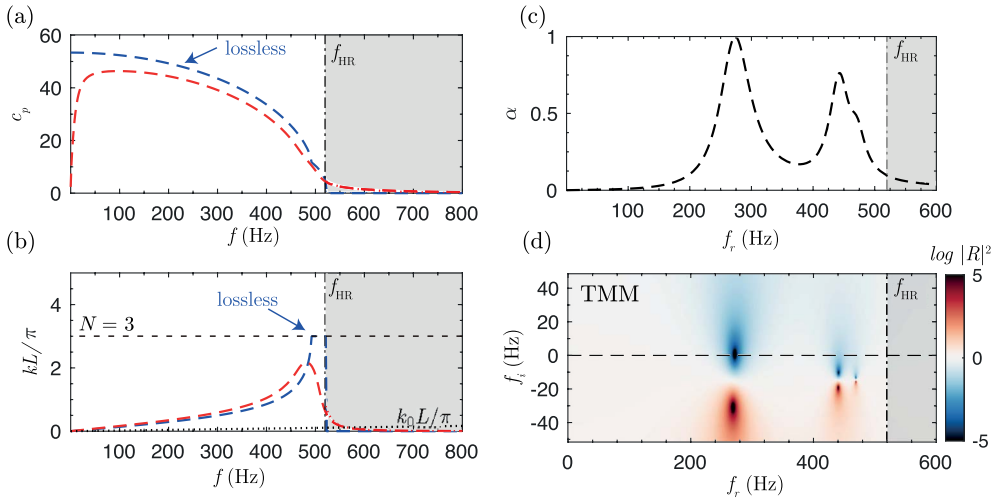

Figure 14. (a) Phase speed for a panel of $N = 3$ resonators calculated by TMM (dashed) for the lossless case (blue) and including thermo-viscous losses (red). (b) Corresponding wavenumber, where k_0 is the wavenumber in air. (c) Absorption of the panel. The dashed-dotted line marks the resonant frequency of the HRs and the shaded area corresponds to the band-gap. (d) Complex-frequency planes of the reflection coefficient calculated by TMM where f_r and f_i are the real and imaginary part of the complex frequency respectively.

the presence of this band gap, slow propagation conditions are achieved in the dispersive band below f_{HR}. In the lossless case, zero phase velocity can be observed for frequencies just below f_{HR}. Note also that the maximum wavenumber inside the slit is limited by the discreteness to the value $k_{max} = \pi N/L$, as shown by the TMM calculations (dashed blue curve in Figure 14(b)). In the lossy case, the losses limit the minimum value of group velocity [61], but in our system slow sound velocity can be achieved in the dispersive band below f_{HR}. The average sound speed in the low frequency range is much lower (50 m/s) than the speed of sound in air.

Consider now the geometry shown in Figure 13(b) where the array is bounded. In that case the frequency of the quarter wavelength resonance, which is $c/4L$ is dictated by the sound velocity of the metamaterial made by the waveguide loaded with the HRs, so by an slow sound velocity. In that case, the resonance frequency is therefore shifted to the low frequencies. Figure 14(c) shows the absorption when the geometry made by $N = 3$ HRs has been tuned to present the exact amount of intrinsic losses that exactly compensates the energy leakage of the system at 275 Hz. In this situation, as shown in Figure 14(d), the lower frequency zero is located on the real axis, leading to a peak of PA. In addition, as we have $N = 3$ resonators, two other secondary peaks of absorption are observed at higher frequencies, e.g. 442 Hz and 471 Hz. Their corresponding zeros are located close to the real axis and, although the critical coupling condition is not exactly fulfilled, high absorption values can be observed at these frequencies.

The previous sample, with $N = 3$ HRs, provides PA for a thickness of $L = 3a = \lambda/34.5$. Using an optimization method (sequential quadratic programming (SQP) method [73]) the geometry of the system can be tuned in order to minimize the thickness of the material, providing structures with PA and deep sub-wavelength dimensions. The TMM was employed in the optimization to consider the discreteness effects on the reflection coefficient. The resulting structure from the optimization procedure is shown in Figure 15(a): a sample with a single layer of resonators, $N = 1$ with $h = 2.63$ mm, $d = 14.9$ cm, $a = L = d/13 = 1.1$ cm, $w_n = 2.25$ mm, $w_c = 4.98$ mm, $l_n = 2.31$ cm, $l_c = 12.33$ cm. The width of the impedance tube used for measurements, d, allows to

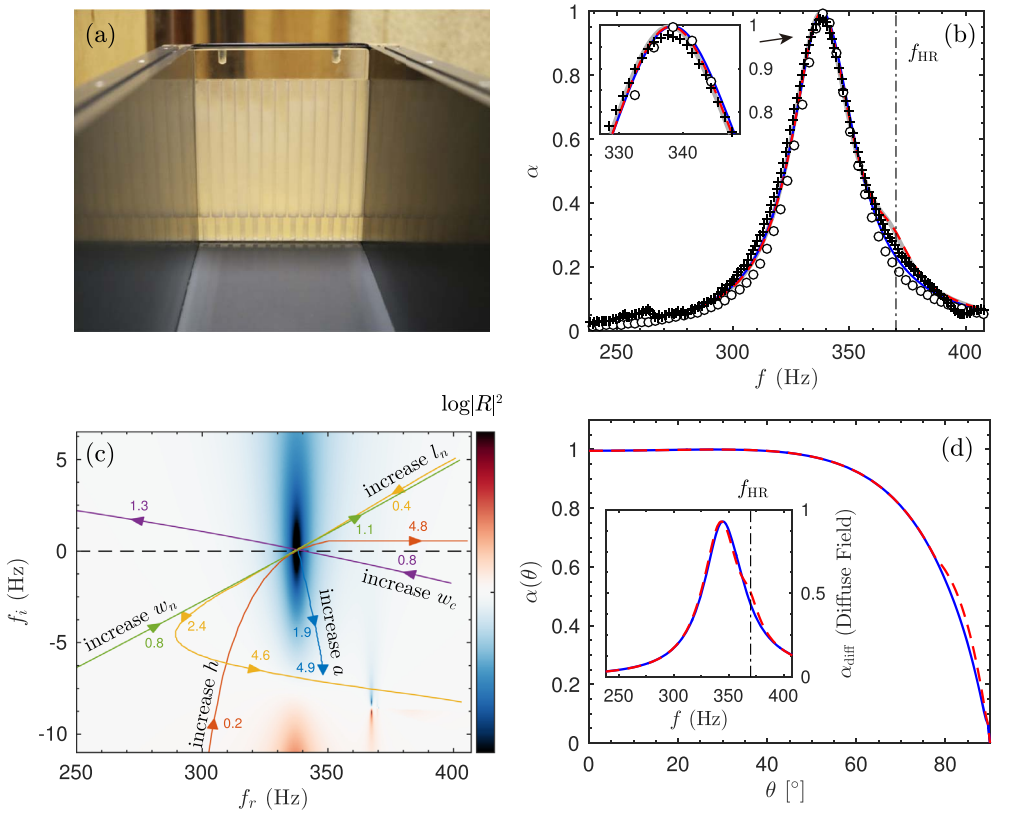

Figure 15. (a) Photograph of the experimental setup with a vertical unit cell, $N = 1$, in the interior of the impedance tube. The translucent resin allows to see the array of HRs. Picture shows the tube open, but it was closed for the experiments. (b) Absorption of the system measured experimentally (crosses), calculated by the full modal expansion (thick continuous gray), effective parameters (dashed red), transfer matrix method (continuous blue) and finite element method (circles). (c) Representation of the reflection coefficient in the complex frequency plane for the optimized sample. Each line shows the trajectory of its zero by changing a geometry parameter. (d) Absorption peak as a function of the angle of incidence calculated by the effective parameters (dashed red), transfer matrix method (continuous blue). The inset in (d) shows the absorption coefficient in diffuse field as a function of frequency. Figure reproduced from Ref. [37].

fit 13 resonators in the transversal dimension as shown Figure 15(a). The sample was built using stereolithography techniques using a photosensitive epoxy polymer.[1] The structure presents a peak of PA at $f = 338.5$ Hz (different than that of the HR, $f_{HR} = 370$ Hz) with a thickness $L = \lambda/88$.

Figure 15(b) shows the absorption coefficient at normal incidence calculated with the different semi-analytical methods, predicted numerically by FEM and measured experimentally. At $f = 338.5$ Hz, PA can be observed. The maximum absorption measured experimentally is $\alpha = 0.97$, as shown in the inset of Figure 15(b). This small discrepancy between the measurements and the models can be caused by experimental reasons including the non perfect fitting of the slit on

[1] (Accura 60®, 3D Systems Corporation, Rock Hill, SC 29730, USA), where the acoustic properties of the solid phase are $\rho_{accura} = 1210$ kg/m^3, $c_{accura} = [1570, 1690]$ m/s.

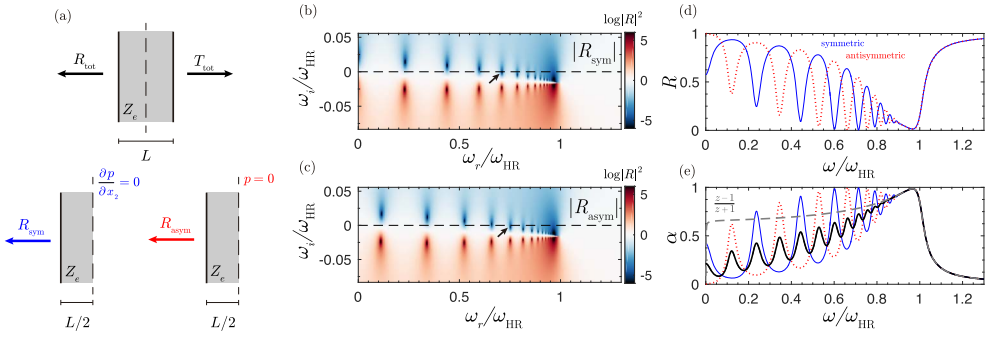

Figure 16. (a) Symmetric and antisymmetric problem decomposition for an homogeneous layer of material with effective parameters. (b–c) Complex frequency representation of the reflection coefficient for the symmetric and antisymmetric problem respectively. (d) Reflection coefficient at the real axis for symmetric (blue) and antisymmetric (dotted red). (e) Absorption for symmetric (blue), antisymmetric (dotted red), total (thick black) and impedance matching condition (dashed gray). Figure reproduced from Ref. [38].

the impedance tube and the excitation of plate modes of the solid medium that composes the metamaterial.

Figure 15(c) also shows the corresponding reflection coefficient in the complex frequency plane. The color map corresponds to the case in which the critical coupling condition is fulfilled, i.e., the zero of the reflection coefficient is exactly located on the real frequency axis. As long as the intrinsic losses depend on the geometry of the resonators and the thickness of the slits, we also represent in Figure 15(c) the trajectory of this zero as the geometry of the system is modified. The crossing of the trajectories with the real frequency axis implies that PA can be achieved with this geometry at this particular frequency. It can be seen that the trajectories linked to the resonators geometry, w_n, w_c, l_n have a strong effect in the real part of the complex frequency of the zero, as they modify the HRs resonant frequency.

Finally, Figure 15(d) shows the absorption of the metamaterial panel as a function of the angle of incidence. It can be observed that almost PA is obtained for a broad range of angles, being $\alpha > 0.90$ for incident waves with $\theta < 60°$. The inset of Figure 15(d) shows the absorption in diffuse field [74] calculated as $\alpha_{\text{diff}} = 2\int_0^{\pi/2} \alpha(\theta)\cos(\theta)\sin(\theta)\,\mathrm{d}\theta$, where at the working frequency it reaches a value of $\alpha_{\text{diff}} = 0.93$, showing the omnidirectional behavior of the absorption in this sub-wavelength structure.

7. Perfect absorption from panels in transmission

In this section we discuss the several possibilities to obtain quasi-PA or PA in the transmission problem, i.e. in the case in which the metamaterial is excited from one side and the wave is either transmitted, reflected or absorbed by the metamaterial. When transmission is introduced, the problem of PA becomes more complicated because the eigenvalues of both the symmetric and the antisymmetric problem must be on the real frequency axis at the same frequency (see Section 4). Depending on the symmetry of the resonator used as building block of the metamaterial, several solutions to the problem are discussed in this section.

7.1. *Quasi-perfect absorption in the symmetric problem by accumulation of resonances*

In this section we theoretically and experimentally report sub-wavelength resonant panels for low-frequency quasi-perfect sound absorption including transmission by using the accumula-

tion of cavity resonances due to the slow sound phenomenon [38]. The sub-wavelength panel is composed of periodic horizontal slits loaded by identical HRs. Due to the presence of the HRs, the propagation inside each slit is strongly dispersive, with near-zero phase velocity close to the resonance of the HRs. In this slow sound regime, the frequencies of the cavity modes inside the slit are down-shifted and the slit behaves as a sub-wavelength resonator. Moreover, due to strong dispersion, the cavity resonances accumulate at the limit of the bandgap below the resonance frequency of the HRs. Near this accumulation frequency, simultaneously symmetric and antisymmetric quasi-critical coupling can be achieved. In this way, using only monopolar resonators quasi-PA can be obtained in a material including transmission.

7.1.1. *Asymptotic behavior, large number of resonators*

Let us first consider N sufficiently large to accurately describe the system as a slab of material with the effective parameters. Figures 16(b–c) show the corresponding reflection coefficient in the complex frequency plane. It is obtained with the TMM, of the symmetric and antisymmetric problems for $N = 30$ resonators considering a complex frequency $\omega = \omega_r + i\omega_i$, with ω_r and ω_i the real and imaginary frequencies. First, it can be observed that a series of zero-pole pairs appear in the frequency complex plane [36]. The poles correspond to the cavity modes inside the slab of effective material [59]. Due to dispersion, these cavity modes accumulate below the resonance frequency of the HRs. It can be also seen that the cavity modes of the symmetric problem (see R_s) appear at frequencies different from the frequencies of the antisymmetric one (see R_a). This effect is clearly seen in Figure 16(d), where the reflection coefficients for each problem are plotted at the real axis of frequencies.

In addition, it can be seen that for some particular frequencies, as those marked with the arrows in Figures 16(b–c), the zeros of the reflection coefficient are located on the real axis of frequencies. At these frequencies, shown by arrows in Figures 16 (b–c), the reflection coefficient of the (anti)symmetric vanishes and the structure is critically coupled. This condition is enough to achieve PA for, e.g., the symmetric problem, as was demonstrated in rigid-backed materials [28, 37, 57]. However, in order to obtain PA of the full transmission problem, both symmetric and antisymmetric reflection coefficients must simultaneously vanish [42, 54], as the following relations hold: $R = (R_s + R_a)/2$ and $T = (R_s - R_a)/2$ as explained in Section 4 and depicted in Figure 16(a).

In general, for a homogeneous slab of material the cavity resonances of the symmetric and antisymmetric problems, i.e., its Fabry–Pérot modes, are staggered in frequency and PA is not possible. However, in our system the cavity modes are accumulated below the limit of the bandgap because of the strong dispersion introduced by the presence of the resonators. Then, the zeros of the reflection coefficient for the symmetric and antisymmetric problems can be close one to another in frequency and quasi-PA can be obtained at the edge of the band-gap. Figure 16(e) shows the corresponding absorption of the full problem (black line), where the absorption due to accumulation of resonances around ω_{HR} is observed. It is interesting to show that, in the limit of a semi-infinite panel, both the reflection coefficient of the symmetric and antisymmetric problems collapse to the impedance matching condition, $\lim_{L\to\infty} R_s = \lim_{L\to\infty} R_a = (Z_e - 1)/(Z_e + 1)$, and then, only in this limit, PA can be achieved, as shown in Figure 16(e). However, for a finite layer $R_s \neq R_a$ and only quasi-PA can be reached with a single homogenized slab of material. Moreover, Z_e is generally complex and no perfect matching can be achieved.

7.1.2. *Finite number of resonators*

Figure 17 shows the scattering of the system in the lossless case for $N = 3$ resonators with the same parameters as in the Section 7.1.1. Figure 17(a–b) shows the complex frequency representation of the reflection coefficient obtained by using the TMM. The TMM correctly accounts for

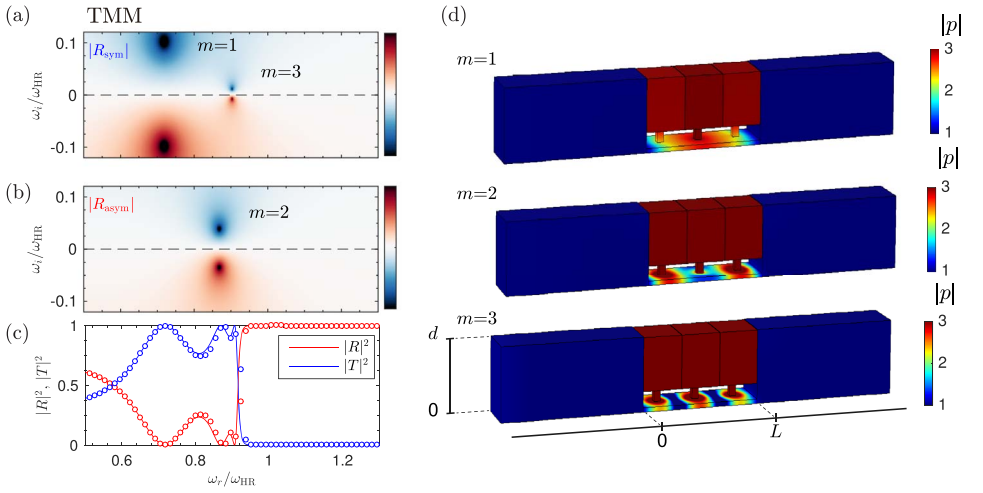

Figure 17. Complex frequency plane representation of the reflection coefficient for a panel of $N = 3$ resonators. (a) Symmetric and (b) asymmetric reflection obtained using the transfer matrix method (TMM). Colorbar in $\log|R|^2$ units. (c) Total transmission (blue) and reflection (red) using TMM, symbols correspond to the FEM simulations. (d) Acoustic field obtained using finite element method (FEM) at frequencies corresponding to the resonances $m = 1,2,3$, colorbar in normalized pressure units.

the finite number of resonances, in this case $N = 3$, in agreement with FEM simulations. It is also worth noting here that these cavity resonances are in fact the collective modes of the HRs and there exist only N different collective modes. Figure 17(c) shows the total reflection and transmission in the real frequency axis calculated with TMM and FEM. We note that the finite number of HRs limits the accumulation of resonances near the band-gap: as N decreases the condition to have symmetric and antisymmetric resonances close to one another in frequency becomes more difficult to achieve. Therefore, the number of (identical) HRs is a critical parameter to obtain quasi-PA in metamaterials made of identical resonators considering transmission by means of the accumulation of resonances.

Once losses are introduced in the system, the zero-pole structure is down shifted in the complex frequency plane and the system starts to absorb energy [36]. Figure 18(a) presents the absorption of a panel as a function of the number of resonators, N, and frequency. First, it can be observed that for a relatively large number of resonators quasi-PA can be achieved even when the discreteness is retained, e.g. for $N = 50$ resonators as shown in the Figure 18(b). The material is almost impedance matched with the exterior medium.

For most sound absorption applications it is desirable to use panels with reduced thickness, and of special interest is the design of panels with sub-wavelength dimensions. Then, when reducing the panel thickness, the number of resonators must also be reduced and, therefore, the accumulation of resonances becomes limited. Figure 18(c) shows the absorption of a panel with $N = 15$ ($L \approx \lambda_{\alpha_{\rm max}}/2$), while Figure 18(d) shows the absorption of a panel with $N = 5$ ($L = \lambda_{\alpha_{\rm max}}/6.6$). In both cases, a peak of absorption is still observed, but its amplitude falls to $\alpha_{\rm max} = 0.96$ and $\alpha_{\rm max} = 0.92$ respectively for each case. The corresponding reflection coefficient in complex frequency plane for $N = 5$ is shown in Figure 18(f) for the symmetric and antisymmetric problems. By tuning the geometry of the system, high acoustic absorption can be achieved by locating one zero of the reflection coefficient of the symmetric problem on the real frequency axis and, simultaneously, locate another zero of the antisymmetric problem as close as possible

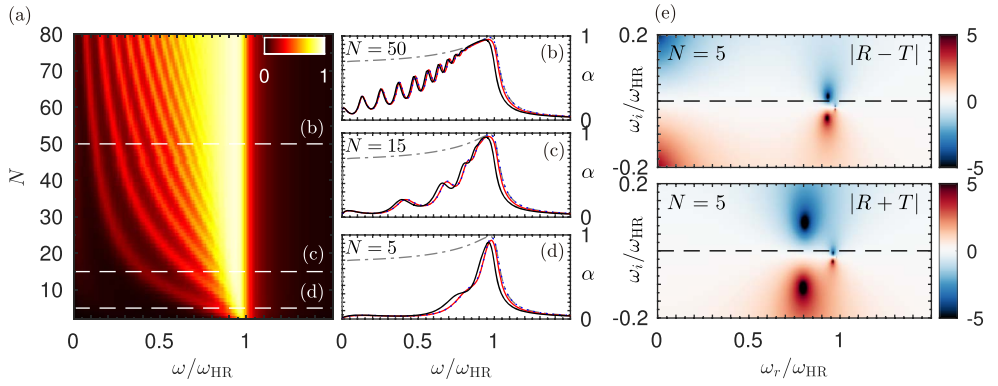

Figure 18. (a) Absorption of the material as a function of the number of resonators and frequency. (b–d) Absorption for $N = 50, 15$ and 5 resonators, obtained using MEM (red), effective parameters (dotted blue) and TMM (black). Dashed-dotted gray line shows the impedance matching condition. (e) Complex frequency representation of the reflection coefficient for $N = 5$ resonators. Colormap in $\log|R|^2$ units. Figure reproduced from Ref. [38].

to the real axis at a different but nearly frequency. Therefore, the maximum value of absorption is directly dependent on the number of HRs and inversely dependent on the panel thickness. Using an array of identical resonators the design of the panel is a compromise between the peak acoustic absorption and the parameter $\lambda_{\max}/L$.

7.1.3. *Experimental results*

A sub-wavelength thickness sample with $N = 10$ resonators is built using stereolithography techniques using a photosensitive epoxy polymer.[2] The geometry of the structure was tuned using an optimization method (sequential quadratic programming (SQP) method [73]) in order to maximize the absorption at a given frequency (350 Hz), while the panel thickness was constrained to $L = \lambda/10$. The resulting parameters were $h = 4.3$ mm, $a = 9.8$ mm, $w_n = 5.3$ mm, $w_{c,1} = 11.4$ mm, $w_{c,2} = 9.3$ mm, $d =$ cm, $l_n = 25.2$ mm, and $l_c = 139.6$ mm. It is worth noting here that we use the coiling of the HRs in order to save space. The amplitude of the acoustic source is low enough to consider negligible the contribution of the nonlinearity of the HRs. Figure 19 summarizes the experimental results. First, Figure 19(a) shows a photograph of the panel, composed by 3 unit cells with $N = 10$ for each one, allowing the measurement of reflection and transmission coefficients at normal incidence (white arrow in Figure 19), which are shown in Figure 19(b). A good agreement between the experimental results, theoretical predictions and FEM simulations is observed. The results show the band-gap generated by the resonance of the HRs, where the low-cutoff frequency of the band-gap is just below the resonance frequency of the HRs, $f_{\rm HR} = 364$ Hz. In this frequency range, transmission almost vanishes and the total reflection does not, as shown in Figure 19(b), as a consequence of the staggered structure of zero-pole structure. The corresponding absorption is plotted in Figure 19(c), where again good agreement can be observed between theory and experiments. Here, at 350 Hz the absorption peak obtained from the experiments was $\alpha = 0.87$, while $\alpha = 0.91$ was obtained from TMM predictions. In addition, small differences can be observed around 300 Hz. These small discrepancies can be associated to imperfections on the fitting of the structure to the impedance tube and due to the coiling of the HRs.

[2] (Accura 60®, 3D Systems Corporation, Rock Hill, SC 29730, USA), where the acoustic properties of the solid phase are $\rho_0 = 1210$ kg/m^3, $c_0 = 1630 \pm 60$ m/s.

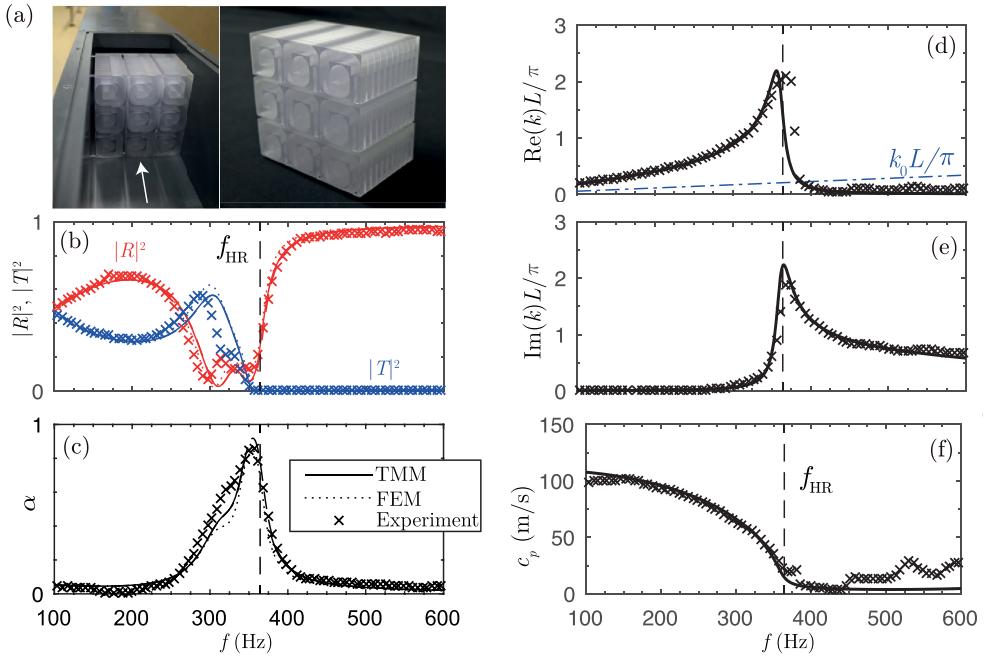

Figure 19. (a) Photographs of the experimental setup, where the semitransparent resin allows to see the coiled HRs inside the material. The arrow shows the incidence direction. (b) Corresponding reflection (red) and transmission (blue) coefficients of the sample measured experimentally (markers), TMM (continuous), and finite element simulation (dotted). The vertical dashed line marks the resonance of the HRs. (c) Corresponding absorption. (d) Real part of the wavenumber (thick gray), and its reconstruction using the experimental data (markers) and analytic data (continuous line). (e) Corresponding imaginary part. (f) Quantity $\tilde{c_p} = \mathrm{Re}(\omega/k)$, closely related to the speed of sound.

The effective wavenumber inside the slits was reconstructed using an inversion method [75]. Figure 19(d,e) shows the experimental and theoretical reconstruction of the real and imaginary part of the wavenumber respectively. It can be observed that the experimental reconstruction agrees with the theoretical prediction. Here, at $f = 350$ Hz where the peak absorption is observed, the real part of the wavenumber is greatly increased compared to the wavenumber in air, k_0. Moreover, the imaginary part of the wavenumber is also increased, leading to the damping of the acoustic waves inside the material. Finally, the quantity $\tilde{c}_p = \mathrm{Re}(\omega/k)$, is shown in Figure 19(f). It can be seen that slow sound conditions are achieved by the experiment and the speed of sound inside the material is reduced to $\tilde{c}_p = 34$ m/s at the peak absorption frequency, $f = 350$ Hz. Finally, it is important to note that the effect of the evanescent coupling between adjacent resonators is negligible. This coupling is implicitly included in FEM simulations and inherently present in the experiments. The good agreement between FEM simulations and experiments, and theoretical models shows the evanescent coupling can be considered negligible.

7.2. *Perfect absorption in asymmetric panels*

In this section we address the problem of the PA in asymmetric panels for a single frequency [39]. The analyzed structure, namely *sub-wavelength asymmetric panel* (SAP) is composed of $N = 2$ HRs and it is shown in Figure 20(a). The SAP is designed to produce a single-frequency peak of PA

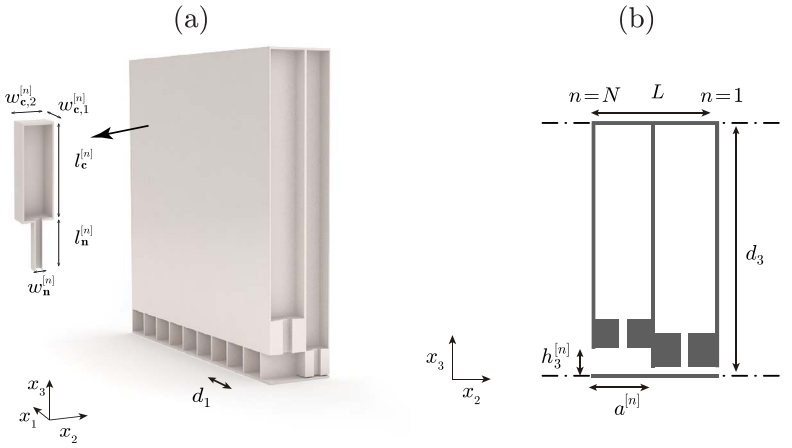

Figure 20. (a) Conceptual view of a sub-wavelength asymmetric panel (SAP) ($N = 2$ resonators), where cross-section shows the waveguide and the loading HRs. (b) Scheme showing the geometrical variables for the SAP.

Table 1. Geometrical parameters for the SAP ($N = 2$)

n	$a^{[n]}$ (mm)	$h_3^{[n]}$ (mm)	$h_1^{[n]}$ (mm)	$l_{\mathbf{n}}^{[n]}$ (mm)	$l_{\mathbf{c}}^{[n]}$ (mm)	$w_{\mathbf{n}}^{[n]}$ (mm)	$w_{\mathbf{c},1}^{[n]}$ (mm)	$w_{\mathbf{c},2}^{[n]}$ (mm)
2	16.8	12.7	13.8	15.4	119.1	4.5	13.8	15.7
1	11.8	1.0	13.8	12.0	134.1	3.2	13.8	10.8

Table reproduced from Ref. [39].

at 300 Hz. The geometrical parameters of both structures were tuned using optimization methods (sequential quadratic programming (SQP) [73]). In the case of the SAP the cost function minimized during the optimization process was $\varepsilon_{\text{SAP}} = |R^-|^2 + |T|^2$, i.e., to maximize the absorption at a given frequency, in this case we selected 300 Hz. The length of the SAP was constrained to $L = 2.64$ cm, i.e., a panel 40 times thinner than the incoming wavelength. The geometrical parameters for the SAP, corresponding to Figure 21, are listed in Table 1 (more details in Ref. [39]). The total structure thickness is $L = \sum a^{[n]} = 28.6$ mm, and its height and width of the unit cell are $d_3 = 148.1$ mm and $d_1 = 14.8$ mm respectively.

We start analyzing the behavior of the designed SAP, considering the two directions of incidence, namely *forward* and *backward*, as depicted in Figures 21(a,b). Figures 21(c–f) show the corresponding absorption, reflection and transmission coefficients for each case. The results are calculated analytically using the transfer matrix method (TMM) in which the thermoviscous losses are accounted for, numerically using finite element method (FEM) and experimentally validated by impedance tube measurements (see Ref. [39] for more details).

First, in the forward configuration, shown in Figure 21(a), the resonator $n = 1$ of the waveguide presents a resonance frequency at $f_1 = 285$ Hz. As a consequence, above f_1, a band gap is introduced and the transmission is strongly reduced, the HR acting effectively as a rigidly-backed wall for the right ingoing waves. Then, the resonator $n = 2$, with a superior resonance frequency at $f_2 = 310$ Hz, is tuned by the optimization process to critically couple the system with the exterior medium, matching the impedance of the waveguide to that of the surrounding medium. This is achieved at 300 Hz. As a consequence, no reflected waves are produced at this particular frequency and therefore, $\alpha = 1 - |R^-|^2 - |T|^2 = 1$ holds. In this situation, PA is observed in a panel

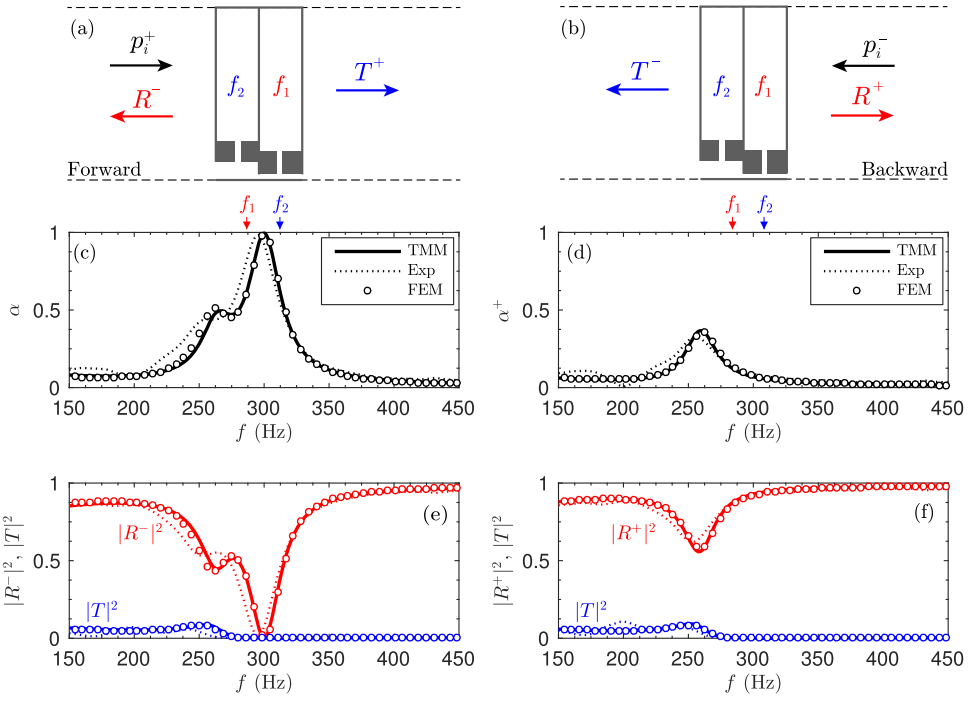

Figure 21. Scheme of the sub-wavelength asymmetric panel in (a) forward and (b) reverse configuration. (c) Absorption for the forward configuration obtained using TMM (continuous line), FEM (circles), and experiment (dotted line). Corresponding reflection and transmission coefficients. (d) Absorption for the backward configuration. (f) Corresponding reflection and transmission coefficients. The arrows mark the resonance frequencies of the HRs, f_1 and f_2. Figure reproduced from Ref. [39].

with a thickness 40 times smaller that the wavelength, i.e., a panel of thickness $L = 2.64$ cm. It is worth noting here that the change of section in the main waveguide helps to achieve the impedance matching, specially for very thin SAPs as the one presented here. We will see later on that this steeped change in the cross-section is analogous to the graded profile of the main waveguide for the broadband structure.

Second, in the backward propagation shown in Figure 21(b), the wave impinges first the lowest resonance frequency resonator, f_1. Now at 300 Hz the wave almost no transmission is allowed in the waveguide. As the waveguide is not impedance matched at 300 Hz in backward direction, reflection is high and absorption is poor ($\alpha^+ = 0.05$). For frequencies below f_2, propagation is allowed in the main waveguide and the effect of the second HR may be visible inducing a decrease of the reflection coefficient. However, the impedance matching in the backward direction is not fully achieved and only a small amount of absorption is observed near the resonance frequency of the first resonator. Therefore, the absorption in this configuration is different from each incidence side.

7.3. *Rainbow absorbers*

The concept of the SAP can be applied to design broadband perfect absorbers. The idea is to create a frequency-cascade of band-gaps and critically coupled resonators in order to generate a rainbow-trapping effect as described in Ref. [39]. By using this approach we address the problem

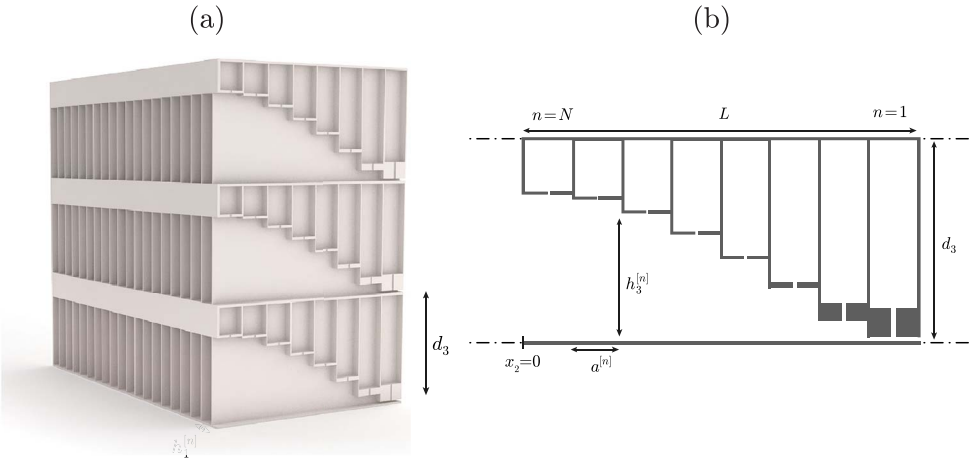

Figure 22. (a) Conceptual view of a sub-wavelength rainbow trapping absorber (RTA) with $N = 8$ HRs, where cross-section shows the waveguide and the loading HRs. (b) Scheme showing the geometrical variables for RTA panels.

of perfect and broadband acoustic absorption using deep-sub-wavelength panels. Rainbow trapping phenomenon, i.e., the localization of energy due to a gradual reduction of the group velocity in graded structures, has been observed in optics [76], acoustics [77–79] or elastodynamics [80]. However, losses were not accounted for and, therefore, absorption was not studied in these works. In the present configuration, a set of graded HRs is used, allowing to reduce, in addition to the thickness of the panels, the dimension of the unit cell to the deep-sub-wavelength regime.

We design panels composed of monopolar resonators with graded dimensions, namely *rainbow-trapping absorbers* (RTA). The designed panels present broadband, perfect and asymmetric sound absorption, and, due to slow sound [32, 38, 39, 57, 81], their thickness is reduced to the deep-sub-wavelength regime. In practice, the resonance frequency of a waveguide in which slow sound propagates is strongly reduced and eventually shifted to the sub-wavelength regime, because it is proportional to the sound velocity. In particular, the structures are composed of a rigid panel, of thickness L, periodically perforated with series of identical waveguides of variable square cross-section loaded by an array of N HRs of different dimensions, as shown in Figures 22(a,b). Each waveguide is therefore divided in N segments of length $a^{[n]}$, width $h_1^{[n]}$ and height $h_3^{[n]}$. The HRs are located in the middle of each waveguide section.

The geometrical parameters are tuned using optimization methods SQP [73]. For the rainbow trapping absorber ($N = 9$), the cost function is $\varepsilon_{\mathrm{RTA}} = \int_{f_1}^{f_N} |R^-|^2 + |T|^2 \,\mathrm{d}f$, i.e., to maximize the absorption in a broad frequency bandwidth, that is chosen from $f_1 = 300$ Hz to $f_N = 1000$ Hz. In the case of the RTA the length of the panel is constrained to $L = 11.3$ cm, i.e. a panel 10 times thinner than the wavelength at 300 Hz. The geometrical parameters for the RTA ($N = 9$), measured experimentally, corresponding to Figure 23, are listed in Table 2 (more details in Ref. [39]). The total structure thickness is $L = \sum a^{[n]} = 113$ mm, and its height and width of the unit cell are $d_3 = 48.7$ mm and $d_1 = 14.6$ mm respectively.

The process is as follows. First, we tune the deepest resonator ($n = 1$) in the waveguide to reduce the transmission above a frequency f_1. Second, in the same way as previously done in the SAP, a second resonator with slightly higher resonance frequency, f_2, is placed in the preceding segment of the waveguide. The geometry of this resonator and the section of the waveguide are tuned to impedance match the system at this frequency. Therefore, the reflection vanishes and a peak of PA is achieved in the same way as in the SAPs. Note this latter HR also reduces the

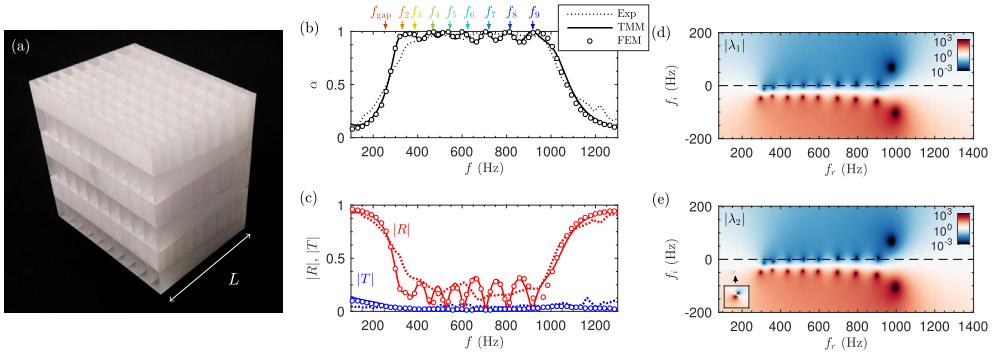

Figure 23. (a) Photograph of the sample containing 10×3 unit cells. (b) Absorption obtained by using the TMM (continuous line), FEM simulations (circles) and measured experimentally (dotted line). (b) Corresponding reflection (red curves) and transmission (blue curves) coefficients in amplitude. (d–e) Complex frequency representation of the eigenvalues of the scattering matrix, $\lambda_{1,2}$. Colormap in $10\log_{10}|\lambda|^2$ scale. Figure reproduced from Ref. [39].

Table 2. Geometrical parameters for the RTA ($N = 9$)

n	$a^{[n]}$ (mm)	$h_3^{[n]}$ (mm)	$h_1^{[n]}$ (mm)	$l_{\mathbf{n}}^{[n]}$ (mm)	$l_{\mathbf{c}}^{[n]}$ (mm)	$w_{\mathbf{n}}^{[n]}$ (mm)	$w_{\mathbf{c},1}^{[n]}$ (mm)	$w_{\mathbf{c},2}^{[n]}$ (mm)
9	7.9	25.6	14.0	1.1	21.4	1.2	14.0	7.2
8	9.5	24.2	14.0	1.0	22.8	1.2	14.0	9.0
7	11.0	22.8	14.0	1.7	23.6	1.4	14.0	10.6
6	12.6	21.6	14.0	0.7	25.9	1.0	14.0	12.0
5	14.1	20.2	14.0	1.5	26.5	1.2	14.0	13.6
4	15.7	18.8	14.0	1.1	28.3	1.0	14.0	15.2
3	17.3	17.4	14.0	1.6	29.2	1.0	14.0	16.8
2	18.8	16.0	14.0	1.1	31.2	0.8	14.0	18.4
1	6.4	1.0	1.0	3.0	44.7	0.6	14.0	5.6

Table reproduced from Ref. [39].

transmission at even higher frequencies. Then, the process can be repeated by extending the waveguide with more segments, each one with a tuned HR being its resonance frequency higher than the preceding one.

Due to machine precision of the available 3D printing system (the minimum step was 0.1 mm), the design of the RTA should be constrained to accomplish this precision. The main limitation is related to the loss of accuracy of the diameters of the small necks that compose the HRs. Under this technological constraint we design the RTA using $N = 9$ HRs and quantizing the dimensions of all the geometrical elements that compose the structure to the machine precision. The manufactured sample is shown in Figure 23(a) and the quantized geometrical parameters are listed in Table 2 (see Ref. [39]). Figures 23(b–c) show the absorption, reflection and transmission of the device calculated with the TMM, FEM and measured experimentally. Note that both reflection and transmission coefficients are plotted in terms of amplitude and not in terms of energy in order to emphasize the fact that the transmission does not vanish apart from the PA frequency band. The deepest resonator ($n = 1$) presents a resonance frequency of $f_1 = f_{\text{gap}} = 259$ Hz, causing the transmission to drop. A set of 9 resonators are tuned following the process

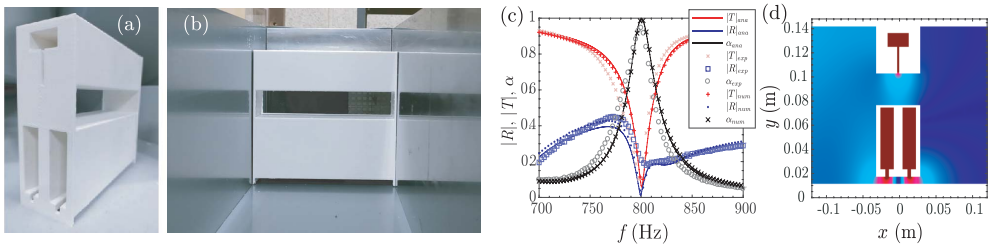

Figure 24. (a,b) Images of the metamaterial with degenerated resonators. (c) Reflection, absorption and transmission coefficients of the metamaterial. (d) Pressure field $|p|$ at the perfect absorption frequency.

previously described, with increasing resonance frequencies ranging from 300 to 1000 Hz. As a result of the frequency-cascade process, the impedance of the structure in the working frequency range is matched with the exterior medium while the transmission vanishes. As a consequence, the RTA presents a flat and quasi-PA coefficient in this frequency range (see Figure 23(b)). Excellent agreement is found between the TMM predictions and FEM simulations, while good agreement is observed between the experimental measurements and both models. It can be observed that at low frequencies there are small differences between the measurements and the models. These disagreements are mainly caused by imperfections in the sample manufacturing, by imperfect fitting of the structure to the impedance tube, by the possible evanescent coupling between adjacent waveguides and adjacent HRs, and/or by the limitations of the visco-thermal model used at the joints between waveguide sections.

The corresponding representation of the two eigenvalues of the **S**-matrix in the complex frequency plane is shown in Figures 23(d–e). We can see that even under the constraints imposed by the metamaterial construction process, all the $N-1$ zeros of the eigenvalues that produce the critical coupling of the structure are located very close to the real axis being the zeros of λ_1 at the same frequencies as λ_2. Note in the manufactured system, not all the zeros are located exactly on the real axis, but the quality factor of the resonances is very low (note the logarithmic color scale in Figure 23(c–d)). Therefore they overlap producing quasi-perfect sound absorption in a frequency band from 300 to 1000 Hz for a panel 10 times thinner than the wavelength at 300 Hz in air.

7.4. *Perfect absorption with mirror symmetric resonators with degenerate resonances*

As previously discussed in Section 4, when the metamaterial is mirror symmetric with respect to its center, degenerated resonators must be used [30,51,54] to achieve perfect absorption. In this section, we show the possibility to design resonant building blocks with different slits supporting each one symmetric and antisymmetric resonances as described in Ref. [51]. Figures 24(a,b) show a mirror-symmetric metamaterial with two slits loaded by one and two HRs. While the slit with a single resonator supports only one single resonance corresponding to the first symmetric Fabry–Pérot resonance, the slit loaded with two HRs supports the first Fabry–Pérot resonances, the first one being symmetric and the second one being antisymmetric. The challenge consists in tuning the symmetric resonance of the slit with a single HR and the antisymmetric resonance of the slit with two HRs at the same frequency with the good amount of inherent losses that compensates the energy leakage. In this case PA can be obtained when a plane wave excites the system independently of the side of the metamaterial, thus producing two-sided PA at the same frequency.

Figure 24(c) shows the scattering coefficients of the full transmission problem. A PA peak is observed at 800 Hz. Figure 24(d) shows the sound field distribution of the complete problem at the perfect absorption frequency. The upper slit, loaded by a single HR, shows a symmetric Fabry–Pérot mode while the lower slit, loaded by two HRs, shows the antisymmetric Fabry–Pérot mode. Both modes are excited at the same frequency, i.e. the structure has a degenerate mode. It should be noted here that perfect absorption is very sensitive to the geometry of the resonators, which explains the slight discrepancies between the analytical or numerical predictions and the experimental results as shown in detail in Ref. [51].

8. Conclusions and perspectives

Finite size acoustic metamaterials made of Helmholtz resonators, or in general, local resonators can be considered as open lossy resonant systems. Due to this open and lossy features, the system can be characterized by both the energy leakage and the inherent losses at the resonance frequency. In this work, only geometries involving the sole propagation of plane waves far from the absorbing system are considered. Then, a scattering matrix of low dimension (1×1 for reflection problems (one port system), 2×2 for transmission problems (two port systems) or 3×3 for the three port system) can be used to represent the scattering properties of the system. The frequencies at which its eigenvalues are zero and the system is excited with the corresponding eigenvector, represent the cases in which the outgoing waves present zero amplitude, and as consequence PA is obtained. We have connected this specific feature situation with the critical coupling condition by means of the representation of the eigenvalues of the scattering matrix in the complex frequency plane [36]. The balance between the energy leakage and the inherent losses of the system, i.e., the critical coupling condition, is graphically represented in the complex frequency plane by the crossing of the zeros of the complex eigenvalues with the real frequency axis, representing the PA configuration. We have used this technique to analyze the reflection problem, where the PA have been obtained in 1-port systems [28] and in reflecting panels [37,57]. The transmission problem becomes more complicated as the zeros of the two eigenvalues should be simultaneously placed on real frequency axis. This situation can be obtained by breaking the symmetry of the system in 2-port systems [42] or in transmission panels [39]. The nonlinear absorption can also be used to fulfill the critical coupling conditions [43, 46]. An intermediate situation can be obtained by using the strong dispersion introduced by the local resonators, producing an accumulation point [38] with quasi-perfect absorption in the transmission problem. The N-port system have been analyzed [53], showing the possibility to obtain the critical coupling conditions for each channel in the system.

The challenge of acoustic absorption and insulation represents a major issue, the solution of which could benefit several industrial sectors such as building, civil or transport ones. Noise reduction and control are major societal and industrial issues, particularly in the low frequency range and require the development of new materials as well as innovative approaches both in terms of process and target properties. Everyday life and industrial standards impose lighter, thinner and long life structures that are needed to mitigate and absorb lower and lower frequency acoustic noises. This work intends to motivate new research lines in the field of acoustic absorption with sub-wavelength structures.

Acknowledgements

The authors gratefully acknowledge the ANR-RGC METARoom (ANR-18-CE08-0021) project and the project HYPERMETA funded under the program Étoiles Montantes of the Région Pays de la Loire. NJ acknowledges financial support from the Spanish Ministry of Science, Innovation

and Universities (MICINN) through grant "Juan de la Cierva-Incorporación" (IJC2018-037897-I). This article is based upon work from COST Action DENORMS CA15125, supported by COST (European Cooperation in Science and Technology).

References

[1] M. Law, L. E. Greene, J. C. Johnson, R. Saykally, P. Yang, "Nanowire dye-sensitized solar cells", *Nat. Mater.* **4** (2005), no. 6, p. 455-459.
[2] A. Derode, P. Roux, M. Fink, "Robust acoustic time reversal with high-order multiple scattering", *Phys. Rev. Lett.* **75** (1995), no. 23, p. 4206-4209.
[3] Y. Chong, L. Ge, H. Cao, A. D. Stone, "Coherent perfect absorbers: time-reversed lasers", *Phys. Rev. Lett.* **105** (2010), no. 5, article ID 053901.
[4] J. Mei, G. Ma, M. Yang, Z. Yang, W. Wen, P. Sheng, "Dark acoustic metamaterials as super absorbers for low-frequency sound", *Nat. Commun.* **3** (2012), article ID 756.
[5] N. Engheta, R. W. Ziolkowski, *Metamaterials: Physics and Engineering Explorations*, John Wiley & Sons, 2006.
[6] V. Romero-García, A. Hladky-Hennion, *Fundamentals and Applications of Acoustic Metamaterials: From Seismic to Radio Frequency*, ISTE Willey, 2019.
[7] R. Craster, S. Guenneau, *Acoustic Metamaterials*, Springer Series in Materials Science, vol. 166, Spinger, 2013.
[8] X. Yu, J. Zhou, H. Liang, Z. Jiang, L. Wu, "Mechanical metamaterials associated with stiffness, rigidity and compressibility: A brief review", *Prog. Mater. Sci.* **94** (2018), p. 114-173.
[9] D. Mu, H. Shu, L. Zhao, S. An, "A review of research on seismic metamaterials", *Adv. Eng. Mater.* **22** (2020), no. 4, article ID 1901148.
[10] Z. Liu, X. Zhang, Y. Mao, Y. Y. Zhu, Z. Yang, C. T. Chan, P. Sheng, "Locally resonant sonic materials", *Science* **289** (2000), no. 5485, p. 1734-1736.
[11] N. Fang, D. Xi, J. Xu, M. Ambati, W. Srituravanich, C. Sun, X. Zhang, "Ultrasonic metamaterials with negative modulus", *Nat. Mater.* **5** (2006), no. 6, p. 452-456.
[12] P. Deymier (ed.), *Acoustic Metamaterials and Phononic Crystals*, Springer-Verlag, Berlin, Heidelberg, 2013.
[13] G. Ma, P. Sheng, "Acoustic metamaterials: From local resonances to broad horizons", *Sci. Adv.* **2** (2016), no. 2, article ID e1501595.
[14] M. Yang, P. Sheng, "Sound absorption structures: From porous media to acoustic metamaterials", *Annu. Rev. Mater. Res.* **47** (2017), p. 83-114.
[15] Y. I. Bobrovnitskii, T. Tomilina, "Sound absorption and metamaterials: A review", *Acoust. Phys.* **64** (2018), no. 5, p. 519-526.
[16] C. Lagarrigue, J.-P. Groby, V. Tournat, O. Dazel, O. Umnova, "Absorption of sound by porous layers with embedded periodic array of resonant inclusions", *J. Acoust. Soc. Am.* **134** (2013), p. 4670-4680.
[17] J.-P. Groby, B. Nennig, C. Lagarrigue, B. Brouard, O. Dazel, V. Tournat, "Enhancing the absorption properties of acoustic porous plates by periodically embedding Helmholtz resonators", *J. Acoust. Soc. Am.* **137** (2015), no. 1, p. 273-280.
[18] C. Lagarrigue, J.-P. Groby, O. Dazel, V. Tournat, "Design of metaporous supercells by genetic algorithm for absorption optimization on a wide frequency band", *Appl. Acoust.* **102** (2016), p. 49-54.
[19] X. Cai, Q. Guo, G. Hu, J. Yang, "Ultrathin low-frequency sound absorbing panels based on coplanar spiral tubes or coplanar Helmholtz resonators", *Appl. Phys. Lett.* **105** (2014), no. 12, article ID 121901.
[20] Y. Li, B. M. Assouar, "Acoustic metasurface-based perfect absorber with deep subwavelength thickness", *Appl. Phys. Lett.* **108** (2016), no. 6, article ID 063502.
[21] Y. Wang, H. Zhao, H. Yang, J. Zhong, J. Wen, "A space-coiled acoustic metamaterial with tunable low-frequency sound absorption", *Europhys. Lett.* **120** (2018), no. 5, article ID 54001.
[22] C. Shen, S. A. Cummer, "Harnessing multiple internal reflections to design highly absorptive acoustic metasurfaces", *Phys. Rev. Appl.* **9** (2018), no. 5, article ID 054009.
[23] Z. Yang, J. Mei, M. Yang, N. Chan, P. Sheng, "Membrane-type acoustic metamaterial with negative dynamic mass", *Phys. Rev. Lett.* **101** (2008), no. 20, article ID 204301.
[24] X. Guo, V. Gusev, K. Bertoldi, V. Tournat, "Manipulating acoustic wave reflexion by a nonlinear elastic metasurface", *J. Appl. Phys.* **123** (2018), no. 12, article ID 124901.
[25] X. Guo, V. Gusev, V. Tournat, B. Deng, K. Bertoldi, "Frequency-doubling effect in acoustic reflection by a nonlinear, architected rotating-square metasurface", *Phys. Rev. E* **99** (2019), article ID 052209.
[26] C. E. Bradley, "Acoustic bloch wave propagation in a periodic waveguide", Tech. rep., Technical Report of Applied Research Laboratories, Report No. ARL-TR-91-19 (July), The University of Texas at Austin (1991).
[27] N. Sugimoto, T. Horioka, "Dispersion characteristics of sound waves in a tunnel with an array of Helmholtz resonators", *J. Acoust. Soc. Am.* **97** (1995), no. 3, p. 1446-1459.

[28] V. Romero-García, G. Theocharis, O. Richoux, A. Merkel, V. Tournat, V. Pagneux, "Perfect and broadband acoustic absorption by critically coupled sub-wavelength resonators", *Sci. Rep.* **6** (2016), article ID 19519.
[29] G. Ma, M. Yang, S. Xiao, Z. Yang, P. Sheng, "Acoustic metasurface with hybrid resonances", *Nat. Mater.* **13** (2014), no. 9, p. 873-878.
[30] M. Yang, C. Meng, C. Fu, Y. Li, Z. Yang, P. Sheng, "Subwavelength total acoustic absorption with degenerate resonators", *Appl. Phys. Lett.* **107** (2015), no. 10, article ID 104104.
[31] Y. Aurégan, "Ultra-thin low frequency perfect sound absorber with high ratio of active area", *Appl. Phys. Lett.* **113** (2018), article ID 201904.
[32] J.-P. Groby, W. Huang, A. Lardeau, Y. Aurégan, "The use of slow waves to design simple sound absorbing materials", *J. Appl. Phys.* **117** (2015), no. 12, article ID 124903.
[33] V. Leroy, A. Strybulevych, M. Lanoy, F. Lemoult, A. Tourin, J. H. Page, "Superabsorption of acoustic waves with bubble metascreens", *Phys. Rev. B* **91** (2015), article ID 020301.
[34] A. A. Fernández-Marín, N. Jiménez, J.-P. Groby, J. Sánchez-Dehesa, V. Romero-García, "Aerogel-based metasurfaces for perfect acoustic energy absorption", *Appl. Phys. Lett.* **115** (2019), article ID 061901.
[35] H. Long, Y. Cheng, J. Tao, X. Liu, "Perfect absorption of low-frequency sound waves by critically coupled subwavelength resonant system", *Appl. Phys. Lett.* **110** (2017), no. 2, article ID 023502.
[36] V. Romero-García, G. Theocharis, O. Richoux, V. Pagneux, "Use of complex frequency plane to design broadband and sub-wavelength absorbers", *J. Acoust. Soc. Am.* **139** (2016), no. 6, p. 3395-3403.
[37] N. Jiménez, W. Huang, V. Romero-García, V. Pagneux, J.-P. Groby, "Ultra-thin metamaterial for perfect and quasi-omnidirectional sound absorption", *Appl. Phys. Lett.* **109** (2016), no. 12, article ID 121902.
[38] N. Jiménez, V. Romero-García, V. Pagneux, J.-P. Groby, "Quasiperfect absorption by subwavelength acoustic panels in transmission using accumulation of resonances due to slow sound", *Phys. Rev. B* **95** (2017), article ID 014205.
[39] N. Jiménez, V. Romero-García, V. Pagneux, J.-P. Groby, "Rainbow-trapping absorbers: Broadband, perfect and asymmetric sound absorption by subwavelength panels for transmission problems", *Sci. Rep.* **7** (2017), no. 1, article ID 13595.
[40] N. Jiménez, T. J. Cox, V. Romero-García, J.-P. Groby, "Metadiffusers: Deep-subwavelength sound diffusers", *Sci. Rep.* **7** (2017), no. 1, article ID 5389.
[41] N. Jiménez, V. Romero-García, J.-P. Groby, "Perfect absorption of sound by rigidly-backed high-porous materials", *Acta Acust. United Acust.* **104** (2018), no. 3, p. 396-409.
[42] A. Merkel, G. Theocharis, O. Richoux, V. Romero-García, V. Pagneux, "Control of acoustic absorption in one-dimensional scattering by resonant scatterers", *Appl. Phys. Lett.* **107** (2015), no. 24, article ID 244102.
[43] V. Achilleos, O. Richoux, G. Theocharis, "Coherent perfect absorption induced by the nonlinearity of a Helmholtz resonator", *J. Acoust. Soc. Am.* **140** (2016), article ID EL94.
[44] H. Long, Y. Cheng, X. Liu, "Asymmetric absorber with multiband and broadband for low-frequency sound", *Appl. Phys. Lett.* **111** (2017), no. 14, article ID 143502.
[45] A. Merkel, V. Romero-García, J.-P. Groby, J. Li, J. Christensen, "Unidirectional zero sonic reflection in passive pt-symmetric willis media", *Phys. Rev. B* **98** (2018), article ID 201102(R).
[46] E. Monsalve, A. Maurel, P. Petitjeans, V. Pagneux, "Perfect absorption of water waves by linearor nonlinear critical coupling", *Appl. Phys. Lett.* **114** (2018), article ID 013901.
[47] L. Schwan, O. Umnova, C. Boutin, "Sound absorption and reflection from a resonant metasurface: Homogenisation model with experimental validation", *Wave Motion* **72** (2017), p. 154-172.
[48] S. Huang, X. Fang, X. Wang, B. Assouar, Q. Cheng, Y. Li, "Acoustic perfect absorbers via spiral metasurfaces with embedded apertures", *Appl. Phys. Lett.* **113** (2018), no. 23, article ID 233501.
[49] A. Elayouch, M. Addouche, A. Khelif, "Extensive tailorability of sound absorption using acoustic metamaterials", *J. Appl. Phys.* **124** (2018), no. 15, article ID 155103.
[50] A. Maurel, J.-F. Mercier, K. Pham, J.-J. Marigo, A. Ourir, "Enhanced resonance of sparse arrays of Helmholtz resonators—application to perfect absorption", *J. Acoust. Soc. Am.* **145** (2019), no. 4, p. 2552-2560.
[51] V. Romero-García, N. Jiménez, J.-P. Groby, A. Merkel, V. Tournat, G. Theocharis, O. Richoux, V. Pagneux, "Perfect absorption in mirror-symmetric acoustic metascreens", *Phys. Rev. Appl.* (2020), article ID 054055.
[52] K. Y. Bliokh, Y. P. Bliokh, V. Freilikher, S. Savel'ev, F. Nori, "Colloquium: Unusual resonators: Plasmonics, metamaterials, and random media", *Rev. Mod. Phys.* **80** (2008), no. 4, p. 1201-1213.
[53] O. Richoux, V. Achilleos, G. Theocharis, I. Brouzos, "Subwavelength interferometric control of absorption in three-port acoustic network", *Sci. Rep.* **8** (2018), no. 1, article ID 12328.
[54] J. R. Piper, V. Liu, S. Fan, "Total absorption by degenrate critical coupling", *Appl. Phys. Lett.* **104** (2014), article ID 251110.
[55] Y. Chong, L. Ge, H. Cao, A. Stone, "Coherent perfect absorbers: Time-reversed lasers", *Phys. Rev. Lett.* **105** (2010), article ID 053901.
[56] P. Wei, C. Croënne, S. T. Chu, J. Li, "Symmetrical and anti-symmetrical coherent prefect absorption for acoustic waves", *Appl. Phys. Lett.* **104** (2014), article ID 121902.

[57] J.-P. Groby, R. Pommier, Y. Aurégan, "Use of slow sound to design perfect and broadband passive sound absorbing materials", *J. Acoust. Soc. Am.* **139** (2016), no. 4, p. 1660-1671.
[58] T. Luk, S. Campione, I. Kim, S. Feng, Y. Jun, S. Liu, J. Wright, I. Brener, P. Catrysse, S. Fan, M. Sinclair, "Directional perfect absorption using deep subwavelength lowpermittivity films", *Phys. Rev. B* **90** (2014), article ID 085411.
[59] V. Pagneux, "Trapped modes and edge resonances in acoustics and elasticity", in *Dynamic Localization Phenomena in Elasticity, Acoustics and Electromagnetism*, CISM International Centre for Mechanical Sciences, vol. 547, Springer, Vienna, 2013, p. 181-223.
[60] M. R. Stinson, "The propagation of plane sound waves in narrow and wide circular tubes, and generalization to uniform tubes of arbitrary cross-sectional shape", *J. Acoust. Soc. Am.* **89** (1991), no. 2, p. 550-558.
[61] G. Theocharis, O. Richoux, V. Romero-Garcìa, A. Merkel, V. Tournat, "Limits of slow sound and transparency in lossy locally resonant periodic structures", *New J. Phys.* **16** (2014), article ID 093017.
[62] J. Kergomard, A. Garcia, "Simple discontinuities in acoustic waveguides at low frequencies: critical analysis and formulae", *J. Sound Vib.* **114** (1987), no. 3, p. 465-479.
[63] V. Dubos, J. Kergomard, A. Khettabi, J.-P. Dalmont, D. Keefe, C. Nederveen, "Theory of sound propagation in a duct with a branched tube using modal decomposition", *Acta Acust. United Acust.* **85** (1999), no. 2, p. 153-169.
[64] F. P. Mechel, *Formulas of Acoustics*, 2nd ed., Springer Science & Business Media, Springer-Verlag, Heidelberg, 2008.
[65] M. Born, E. Wolf, *Principles of Optics: Electromagnetic Theory of Propagation, Interference and Diffraction of Ligth*, Cambridge University Press, UK, 1999.
[66] C. Zwikker, C. Kosten, *Sound Absorbing Materials*, Elsevier Publishing Company, Amsterdam, 1949.
[67] Q. Xu, S. Sandhu, M. L. Povinelli, J. Shakya, S. Fan, M. Lipson, "Experimental realization of an on-chip all-optical analogue to electromagnetically induced transparency", *Phys. Rev. Lett.* **96** (2006), article ID 123901.
[68] X. Yang, M. Yu, D.-L. Kwong, C. W. Wong, "All-optical analog to electromagnetically induced transparency in multiple coupled photonic crystal cavities", *Phys. Rev. Lett.* **102** (2009), article ID 173902.
[69] E. H. E. Boudouti, T. Mrabti, H. Al-Wahsh, B. Djafari-Rouhani, A. Akjouj, L. Dobrzynski, "Transmission gaps and Fano resonances in an acoustic waveguide: analytical model", *J. Phys.: Condens. Matter* **20** (2008), article ID 255212.
[70] A. Santillan, S. I. Bozhevolnyi, "Acoustic transparency and slow sound using detuned acoustic resonators", *Phys. Rev. B* **84** (2011), article ID 064394.
[71] A. Mouadili, E. H. E. Boudouti, A. Soltani, A. Talbi, B. Djafari-Rouhani, A. Akjouj, K. Haddadi, "Electromagnetically induced absorption in detuned stub waveguides: a simple analytical and experimental model", *J. Phys.: Condens. Matter* **26** (2014), article ID 505901.
[72] Y. Xu, Y. Li, R. K. Lee, A. Yariv, "Scattering-theory analysis of waveguide–resonator coupling", *Phys. Rev. E* **62** (2000), p. 7389-7404.
[73] M. J. Powell, "A fast algorithm for nonlinearly constrained optimization calculations", in *Numerical Analysis*, Springer, 1978, p. 144-157.
[74] T. J. Cox, P. D'Antonio, *Acoustic Absorbers and Diffusers: Theory, Design and Application*, 3rd ed., CRC Press, 2016.
[75] J.-P. Groby, E. Ogam, L. De Ryck, N. Sebaa, W. Lauriks, "Analytical method for the ultrasonic characterization of homogeneous rigid porous materials from transmitted and reflected coefficients", *J. Acoust. Soc. Am.* **127** (2010), no. 2, p. 764-772.
[76] K. L. Tsakmakidis, A. D. Boardman, O. Hess, "Trapped rainbow storage of light in metamaterials", *Nature* **450** (2007), no. 7168, p. 397-401.
[77] J. Zhu, Y. Chen, X. Zhu, F. J. Garcia-Vidal, X. Yin, W. Zhang, X. Zhang, "Acoustic rainbow trapping", *Sci. Rep.* **3** (2013), article ID 1728.
[78] V. Romero-Garcia, R. Picó, A. Cebrecos, V. Sanchez-Morcillo, K. Staliunas, "Enhancement of sound in chirped sonic crystals", *Appl. Phys. Lett.* **102** (2013), no. 9, article ID 091906.
[79] X. Ni, Y. Wu, Z.-G. Chen, L.-Y. Zheng, Y.-L. Xu, P. Nayar, X.-P. Liu, M.-H. Lu, Y.-F. Chen, "Acoustic rainbow trapping by coiling up space", *Sci. Rep.* **4** (2014), article ID 7038.
[80] A. Colombi, D. Colquitt, P. Roux, S. Guenneau, R. V. Craster, "A seismic metamaterial: The resonant metawedge", *Sci. Rep.* **6** (2016), article ID 27717.
[81] A. U. Jan, R. Porter, "Transmission and absorption in a waveguide with a metamaterial cavity", *J. Acoust. Soc. Am.* **144** (2018), no. 6, p. 3172-3180.